Characterization of Silicone Polymers for Energy Harvesting from Compliant Membrane Foils

Albin Wells

Submitted on: 4 April 2021

Submitted in partial fulfillment of the requirements of the degree of Bachelor of Science with Honors in Mechanical Engineering

School of Engineering, Brown University

Prepared under the direction of
Prof. Kenneth Breuer, Advisor
Prof. Allan Bower, Reader

By signing below, I attest that the undergraduate thesis listed above meets the criteria for Honors, and has been successfully presented to the faculty at the Undergraduate Research Symposium.

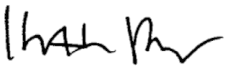

Advisor's Signature

A.F. Bower

Reader's Signature

Honors Chair's Signature

1.0 Abstract

Within the field of hydrokinetic energy harvesting, passive membranes have shown promise as devices suitable for energy capture. As much about the behavior of shape-morphing foils is still largely unknown, this project develops from previous work analyzing how compliant membranes can be employed to maximize the efficacy of tidal flow energy harvesting. This work investigates the silicone elastomers used for these compliant foils, combining a series of uniaxial tests, ring-down experiments, and computational modelling to comprehensively characterize the material. These findings will be used to predict and understand how the material behaves as a hydrodynamic foil in energy harvesting applications. Furthermore, the approach provides a simple and cost-effective method for characterizing similar hyperelastic materials. The work shows the potential of a mechanical oscillator to estimate the elastic modulus at a given strain and the damping coefficient for hyperelastic materials with some viscoelastic properties. This method can quickly be employed to estimate both of these values utilizing readily available tools, and effectively characterize nonlinear, hyperelastic materials.

2.0 Introduction

As the carbon concentrations in our atmosphere continue to increase, the negative effects associated with anthropogenic climate change will only become more profound. Increased global temperatures pose a threat to all sources of life: as unpredictable weather patterns disrupt ecosystems across the globe, rising sea levels flood coastal regions, and warming oceans endanger aquatic life. With over 75% of all greenhouse gas emissions resulting from fossil fuel consumption, there is a dire need to meet the global energy demand with renewable energy sources.[1]

Within the sphere of sustainable energy harvesting, the capacity of hydropower as a source of energy is immense. The potential of rigid foils in hydrokinetic energy extraction has become widely accepted as a promising area in energy harvesting from low-velocity, high-volume flows. Oscillating hydrodynamic foils represent a minimally invasive, more robust, and versatile source of renewable energy compared to standard rotary turbines. Not only do they reduce the impact on marine environments, they can also be deployed in shallower water, and can harvest tidal current energy from the entire span of a channel. While these rigid foils struggle to match the efficiency of standard rotary turbines, passive shape-morphing ‘compliant’ foils offer a way to bridge this gap. The ability for the hydrodynamic foil material to camber and interact with the flow generates stable leading edge vertices (LEVs), which increases the lift forces driving the foil. Initial research shows that silicone-based polymer membrane foils can increase the efficiency up to 260% compared to rigid foils.[2]

While preceding work has focussed on the fluid-foil interactions–analyzing LEV formation and shedding–the material properties of the silicone polymer membranes used for the foils has not

been fully defined. Thus, the relationship between material behavior and experimental conditions cannot be fully understood. The idea of this work is to adequately characterize the material and to gain a comprehensive understanding of its properties through a series of static uniaxial experiments and dynamic oscillation ring-down method. These realizations could help establish a connection between optimal energy harvesting conditions and hydrofoil material properties, and explain phenomena seen in future experiments and ultimately during the implementation of such foils in tidal waters. Furthermore, the viscoelastic behavior of silicone polymers could lead to energy losses that limit the foil efficiency: the relevance and magnitude of these losses need to be properly identified as well.

In general, this work has implications beyond its intrinsic scope. The procedures carried out represent straightforward and cost efficient methods that serve as a template for the study of similar hyperelastic material studies. This is especially relevant when access to expensive machinery is limited, as the procedures utilize accessible and common materials. Similar rubber-like, hyperelastic materials that can be studied using this method are materials with long-term flexibility under a variety of loads, and have applications as car tires or door seals, among other uses.

3.0 Background

3.1 Silicone Polymer Material

Silicone rubbers are used in a wide variety of products and technologies, ranging from household, domestic objects to advanced, high-performance technologies.[3] The favorable material properties of silicone elastomers such as a resistance to tearing, thermal and electrical resistance, robustness, and overall material strength and longevity lend themselves to large ranges of applications. In our case, this material is used as a compliant membrane in hydrodynamic foils for energy harvesting.[4]

The specific characteristics of silicone polymers can easily be altered and manipulated for the desired use. In order to obtain the solid silicone polymer material desired, uncured liquid silicone must be cross-linked to form a covalent polymer network. Liquid silicone undergoes platinum-based addition curing reaction called hydrosilylation, in which a polymer base is mixed with a diluted crosslinker. Each premixed part, ambiguously labeled ‘Part A’ or ‘Part B’, is stable and unreactive. The dilution of the cross-linked part is essential in preventing immediate, local curing and inconsistencies in the overall material shape and strength.

Contrary to standard polymers with a carbon spine, silicone rubbers consist of alternating silicone and oxygen units in their backbone. This unique backbone structure accounts for many of its advantageous properties including high flexibility, softness, and thermal stability. This backbone is bonded to methyl groups (CH_3). The entire structure is shown in Figure 3.1 below.

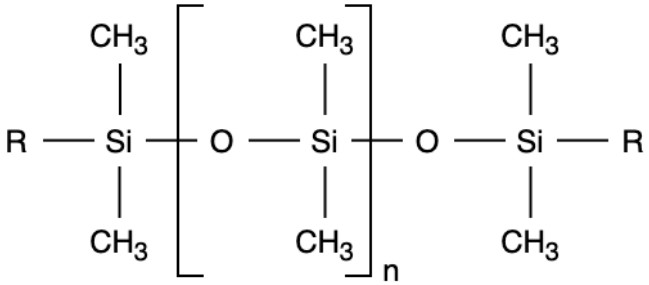

Figure 3.1. Silicone polymer molecular structure

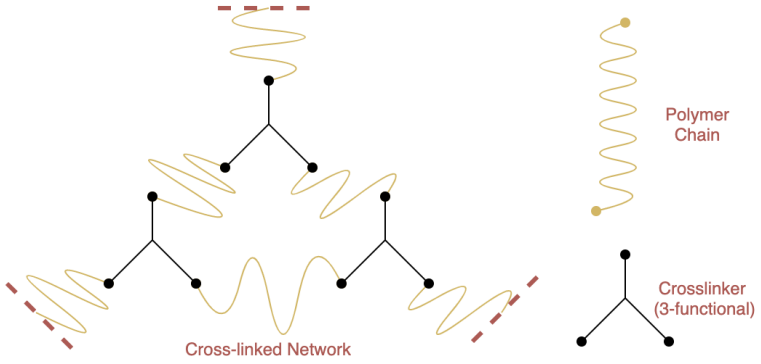

Figure 3.2. Ideally linked silicone network structure

The ideal silicone polymeric network is represented by a grid structure with cross-linkers connecting polymer chains (Figure 3.2). The effects of this grid structure can be envisioned by viewing these polymer chains as springs. Denser cross-linking will increase the number of spring units per area, which in turn increases the material strength. In general, the stiffness of this system of springs is the Young's modulus, E, which is proportional to the material density. This serves as the basis of Hooke's law:

$$\sigma = E\varepsilon \tag{1}$$

Assuming incompressibility, the Young's modulus is related to shear modulus, μ:

$$E = 2\mu(1 + \nu) = 3\mu \tag{2}$$

Note that the incompressibility assumption, which indicates no change in volume under deformation, is standard for rubber-like materials and is represented by a Poisson's ratio, ν, of 0.5. For silicone elastomers, Hooke's law only holds true in the linear region, up to 10% strain. Beyond this small initial region, the onset of strain-softening and strain-hardening phenomena create a non-linear stress-strain relationship. Ultimately, these materials can reach strains well beyond 300-400% (in some cases exceeding 1000%) and stresses around 1 MPa (reaching up to 13 MPa).[5]

For non-ideal elastomers, the relationship between stress and strain is more complicated due to a dependence on strain rate. Moreover, many commercially available silicone polymers include the presence of various fillers, which enhance the material tear strength and tensile properties but

further contribute to some complex, non-linear phenomena. This includes the Mullins effect, which indicates changing stress-strain curves under steady-state, cyclic loading at increasing or decreasing maximum strains.[4] This effect shows that, when the material is stretched beyond a previous maximum stretch, it becomes softer. Subsequently, the permanent set of filled elastomers shows elastomer elongation following static stretching for an extended period of time. This results from a reorganization and curing within the material, so that it reaches a new zero-stress molecular state. However, this effect is not necessarily permanent and the material can return to its original zero-stress state over time. Finally, the Payne effect is also noticeable in filled silicone elastomers. The effect shows a shift in shear modulus as strain increases. The phenomena indicates an initial material storage modulus at low strains (<1%), followed by a rapid decrease in modulus due to breaking macromolecules into subnetworks, and ultimately a constant storage modulus exceeding around 10-20% strain.[6] In turn, the governing equation (2) above can be rewritten to include influences from these effects under small strains:

$$\sigma(\varepsilon, \frac{d\varepsilon}{dt}) = f(\varepsilon) \cdot g(\varepsilon, \frac{d\varepsilon}{dt}) \cdot h(\varepsilon, \varepsilon_{max}) \tag{3}$$

where $f(x)$ is the simple linear relationship from (2), $g(\varepsilon, \frac{d\varepsilon}{dt})$ indicates a dependence on the strain rate from the Payne effect, and $h(\varepsilon, \varepsilon_{max})$ captures softening due to the Mullins effect.

As the Mullins effect, Payne effect, and permanent set can cause substantial changes in data repeatability and consistency, caution must be taken during experimentation to identify if these effects are present and how they might affect results. In general, some precautions can be taken to minimize these nonlinear phenomena. Ample rest time should be given to reduce the impact of the permanent set, and elastomers should be stretched significantly (beyond what will be experienced during testing) to ensure they have already experienced the maximum strain. Finally, some elastomers with a strong Payne effect will soften at a specific strain rate–this should also be addressed and looked out for.[7]

3.2 Material Modelling

The modeling of various phenomena observed in materials is the basis of understanding and predicting material behavior. Furthermore, accurate material modelling and prediction can aid in the design and development of new materials for specific applications. Although the concept of material modeling is centuries old, it remains a dynamic field, with new models constantly being proposed and optimized.

Although silicone rubbers possess both viscous and elastic behaviors, the effects are dominated by the elastic contributions. Thus, viscous effects can be negated entirely if strain rates are not too high. Under this assumption, hyperelastic models can be used to define and fit data. Additionally, filled elastomers tend to behave as hyperelastic materials and are commonly modeled as such.[8] Choosing a model is not always trivial, as each has advantages and drawbacks for different types of hyperelastic materials. In general, however, these models all aim

to capture the non-linear stress-strain relationship observed for hyperelastic materials in a given strain range. These models can be split into categories as mechanistic models that derive equations from underlying material mechanics, phenomenological models that describe observed properties, and hybrid models containing mechanistic and phenomenological aspects. Note that, for soft, rubber-like materials, we will assume incompressibility.[9]

3.2.1 Overview: General Methods

A few overarching methods form the basis of all hyperelastic models. Although these relationships are well known and outlined in textbooks covering hyperelasticity, they are nonetheless important to restate here for completeness and understanding. Overall, the upcoming sections follow the frameworks outlined in *Applied Mechanics of Solids*[10], *Mechanics of Solid Polymers*[17], and a publication on the assessment of hyperelastic material models[9].

In general, hyperelastic materials can be explained by the relationship between strain energy, W, and strain invariants, I_1, I_2, and I_3. All of these models start from the relation

$$W = f(I_1, I_2, I_3) \tag{3}$$

which ensures perfectly elastic material behavior. These invariants are equivalent to various combinations of the principal extensions, λ_1, λ_2, and λ_3:

$$I_1 = \lambda_1^2 + \lambda_2^2 + \lambda_3^2 \tag{4}$$

$$I_2 = \lambda_1^2\lambda_2^2 + \lambda_2^2\lambda_3^2 + \lambda_3^2\lambda_1^2 \tag{5}$$

$$I_3 = \lambda_1^2\lambda_2^2\lambda_3^2 \tag{6}$$

$$\lambda = \varepsilon + 1 \tag{7}$$

Furthermore, assuming incompressibility and uniaxial extension, we can further obtain the following relationships 8 and 9, respectively:

$$\lambda_1\lambda_2\lambda_3 = 1 \tag{8}$$

$$\lambda_1 = \lambda,\ \lambda_2 = \lambda_3 = \frac{1}{\sqrt{\lambda}} \tag{9}$$

Equations 8 and 9 hold true during uniaxial testing, and are used to derive the uniaxial stress-strain relations for each model. The general form for particular models are guided by experiments, but all include variables that can be used to define a particular material. For each model, materials are assumed to be isotropic; this means that material behavior is independent of orientation with respect to loading. Ultimately, particular stress-strain relationships for every model are obtained by differentiating the strain energy density.[10]

3.2.2 Mechanistic Models

One of the simplest hyperelastic constitutive models available is the neo-Hookean model.[11] This model is similar to Hooke's law yet predicts nonlinear behavior of certain materials at larger strain rates. The neo-Hookean model is accurate for various cross-linked polymer materials. Initially, at low strains, polymer chains can move relatively freely but eventually the chain will be stretched to a maximum point and the cross-links will prevent further stretching. Thus, the

model shows a gradual increase in the elastic modulus of a material. This model can be used for rubber-like materials during the initial linear range (usually below 20% strain), but is generally known to be inaccurate in predicting phenomena at higher strains.[12][13] The strain energy density, W, for a neo-Hookean solid is:

$$W = \frac{\mu_1}{2}(\bar{I}_1 - 3) + \frac{K_1}{2}(J-1)^2 \tag{10}$$

where μ_1 and K_1 are material constants and $\bar{I}_1$ is the deviatoric first invariant of the left Cauchy-Green deformation tensor (note that $\bar{I}_1 = J^{-2/3} I_1$). The stress-strain relationship is as follows:

$$\sigma = \frac{\mu_1}{J^{5/3}}(J^{-2/3}B - \tfrac{1}{3}\bar{I}_1 I) + K_1(J-1)I \tag{11}$$

where B is the left Cauchy-Green deformation tensor, I is the identity matrix, and J is the Jacobian of the deformation gradient. For incompressibility, J must be 1 to preserve volume. For isotropic, incompressible materials, the uniaxial stress-stretch relation can be derived by finding the Cauchy stress differences (assuming incompressibility) and assuming no traction:

$$\sigma_{11} - \sigma_{33} = \lambda_1 \frac{dW_1}{d\lambda_1} - \lambda_3 \frac{dW_3}{d\lambda_3} \text{ and } \sigma_{22} - \sigma_{33} = \lambda_2 \frac{dW_2}{d\lambda_2} - \lambda_3 \frac{dW_3}{d\lambda_3} \tag{12}$$

$$\frac{dW_i}{d\lambda_i} = \mu_1 \lambda_i$$

$$\sigma_{11} - \sigma_{33} = \mu_1(\lambda_1^2 - \lambda_3^2) \text{ and } \sigma_{22} - \sigma_{33} = \mu_1(\lambda_2^2 - \lambda_3^2) = 0$$

$$\sigma_{11} = \sigma = \mu_1(\lambda^2 - \tfrac{1}{\lambda}) \text{ since } \sigma_{22} = \sigma_{33} = 0 \text{ (no traction)}$$

$$\sigma_{Eng} = \frac{\sigma}{\lambda} = \mu_1(\lambda - \frac{1}{\lambda^2}) \tag{13}$$

where σ_{Eng} is nominal stress.

A more complex mechanistic model is the Arruda-Boyce 'eight-chain' model.[14][15] The Arruda-Boyce model is motivated by the microstructure of rubber-like polymers. The model is based on a volume element with eight polymer chains, with each chain linking on a diagonal from a corner. The strain energy density is given by:

$$W = \mu(\tfrac{1}{2}(\bar{I}_1 - 3) + \frac{1}{20\beta^2}(\bar{I}_1^2 - 3^2) + \frac{11}{1050\beta^4}(\bar{I}_1^3 - 3^3) + ...) + \frac{K}{2}(J-1)^2 \tag{14}$$

where μ, β, and K are material properties. The Cauchy stress for the Arruda-Boyce model for an incompressible solid is:

$$\sigma = \mu(1 + \frac{I_1}{5\beta^2} + \frac{33{I_1}^2}{175\beta^4} + ...)B \tag{15}$$

Furthermore, the uniaxial stress can be derived as:

$$\sigma_{11} = \sigma = \mu(\lambda^2 - \tfrac{1}{\lambda})(1 + \frac{I_1}{5\beta^2} + \frac{33{I_1}^2}{175\beta^4} + ...) = C(\lambda^2 - \tfrac{1}{\lambda})$$

$$\sigma_{Eng} = \frac{\sigma}{\lambda} = C(\lambda - \frac{1}{\lambda^2}) \tag{16}$$

where $C = \mu(1 + \frac{I_1}{5\beta^2} + \frac{33{I_1}^2}{175\beta^4} + ...)$. Recall that, from our general methods and assumptions above, $I_1 = \lambda^2 - \frac{2}{\lambda}$, so C is variable with a dependence on stretch. Under small deformation, the

material property μ can be taken as the shear modulus. Initial shear modulus can be related to shear modulus by:[16]

$$\mu_0 = \mu(1 + \frac{3}{5\beta^2} + \frac{99}{175\beta^4} + \frac{513}{875\beta^6} + \frac{42039}{67375\beta^8}) \quad (17)$$

The Arruda-Boyce model is advantageous under high stretch conditions. The model only requires three input parameters (including the bulk modulus, K) and has no dependence on the second invariant, I_2. It is similar in accuracy to the Gent model.[17]

3.2.3 Phenomenological Models

The Mooney-Rivlin model is a two parameter phenomenological model that essentially aims to improve the accuracy of the Neo-Hookean model.[9][10][18] As a result, the Mooney-Rivlin model is a linear combination of two invariants of the left Cauchy-Green deformation tensor, as opposed to only one like the Neo-Hookean model. The strain energy density is:

$$W = \frac{\mu_1}{2}(\bar{I}_1 - 3) + \frac{\mu_2}{2}(\bar{I}_2 - 3) + \frac{K_1}{2}(J-1)^2 \quad (18)$$

where μ_1, μ_2, and K_1 are material constants Note that the first invariant of the left Cauchy-Green deformation tensor $\bar{I}_1 = J^{-2/3}I_1$ and the second invariant $\bar{I}_2 = J^{-4/3}I_2$. For an incompressible Mooney-Rivlin solid:

$$\sigma = (\mu_1 + I_2\frac{\mu_2}{2})B - \mu_2 B \cdot B - \frac{1}{3}(\mu_1 I_1 + 2\mu_2 I_2)I \quad (19)$$

In the case of uniaxial tension, a similar derivation utilizing Cauchy stress difference shown in Equation 12 with simplification outlined in Equation 9 can be used to show:

$$\sigma_{11} = \sigma = (\mu_1 + \frac{\mu_2}{\lambda})(\lambda^2 - \frac{1}{\lambda})$$
$$\sigma_{Eng} = \frac{\sigma}{\lambda} = (\mu_1 + \frac{\mu_2}{\lambda})(\lambda - \frac{1}{\lambda^2}) \quad (20)$$

In the case of a Mooney-Rivlin solid under small strains, the shear modulus, μ, can be related to the equation by:

$$\mu = \mu_1 + \mu_2 \quad (21)$$

This two-parameter model is particularly useful in obtaining a value for shear modulus, yet the model can become inaccurate at strains above 100%.

The Yeoh model, also known as the reduced polynomial model, is another model for nonlinear materials that is only dependent on the first strain invariant, I_1 (for incompressible materials).[9] It is given by:

$$W = \sum_{i=1}^{N} C_{i0}(\bar{I}_1 - 3)^i + \sum_{k=1}^{N} \frac{1}{D_k}(J-1)^{2k} \quad (22)$$

where C_{i0} and D_k are material properties. Solving for uniaxial stress for $N = 3$ and assuming incompressibility:

$$\sigma = 2\frac{dW}{dI_1}B \text{ where } \frac{dW}{dI_1} = \sum_{i=1}^{N} iC_i(I_1 - 3)^{i-1} \quad (23)$$

$$\sigma_{11} = \sigma = 2(\lambda^2 - \frac{1}{\lambda}) \sum_{i=1}^{N} iC_{i0}(I_1 - 3)^{i-1}$$

$$\sigma = 2(\lambda^2 - \frac{1}{\lambda})(C_{10} + 2C_{20}(\lambda^2 + \frac{2}{\lambda}) + 3C_{30}(\lambda^2 + \frac{2}{\lambda})^2)$$

$$\sigma_{Eng} = \frac{\sigma}{\lambda} = 2(\lambda - \frac{1}{\lambda^2})(C_{10} + 2C_{20}(\lambda^2 + \frac{2}{\lambda}) + 3C_{30}(\lambda^2 + \frac{2}{\lambda})^2) \quad (24)$$

In the Yeoh model, C_{10} must be a positive value and can be interpreted as half of the shear modulus, $\mu = 2C_{10}$. For curve-fitting purposes, it is generally a rule-of-thumb to take $C_{20} \approx -0.01C_{10}$ and $C_{30} \approx -0.01C_{20}$. In order to take advantage of superior aspects of the Yeoh model, a value of $N = 3$ is typical and effective for most practical applications, and is hence the solution shown above. It can be noticed that, when $N = 1$ the equation is equivalent to the neo-Hookean model.[17]

Finally, the Ogden model is a phenomenological hyperelastic form that is directly based on principal stretch ratios instead of strain invariants.[10][17][19] It follows the form:

$$W = \sum_{i=1}^{N} \frac{2\mu_i}{\alpha_i^2}(\overline{\lambda}_1^{\alpha_i} + \overline{\lambda}_2^{\alpha_i} + \overline{\lambda}_3^{\alpha_i} - 3) + \frac{K_1}{2}(J - 1)^2 \quad (25)$$

where μ_i, a_i, and K_1 are material properties, and $\overline{\lambda_i} = \lambda_i J^{-2/3}$. While the general solution to obtain the stress is lengthy, it follows the same formula: deriving strain energy density with respect to each principal stretch. Important to note with the Ogden model, is that for $N = 1$ and $\alpha = 2$, the formula is identical to the neo-Hookean form. Furthermore, for $N = 2$, $\alpha_1 = 2$ and $\alpha_2 = -2$, the model reduces to the Mooney-Rivlin form. For an incompressible material under uniaxial tension, the Ogden stress takes the from:

$$\sigma_1 = \sigma = \sum_{i=1}^{N} \mu_i(\lambda^{\alpha_i} - \lambda^{-\frac{1}{2}\alpha_i})$$

$$\sigma_{Eng} = \frac{\sigma}{\lambda} = \sum_{i=1}^{N} \frac{\mu_i}{\lambda}(\lambda^{\alpha_i} - \lambda^{-\frac{1}{2}\alpha_i}) \quad (26)$$

Under small strains, the shear modulus, μ, is:

$$\mu = \sum_{i=1}^{N} \mu_i \quad (27)$$

The Ogden form has shown strong correlations with uniaxial testing data for large strains, being accurate up to 700% if an appropriate material is being modeled with proper parameters.[19]

3.2.4 Hybrid Models

The Gent model is based on the concept of limiting polymer network stretch.[9][20] In this aspect, it is similar to the Arruda-Boyce model. The Gent model is aimed at characterizing materials under large deformation. The constitutive equation is:

$$W = -\frac{\mu J_m}{2} ln(1 - \frac{I_1 - 3}{J_m}) + \frac{K}{2}(\frac{J^2 - 1}{2} - ln(J)) \quad (28)$$

where μ, J_m, and K are shear modulus, a dimensionless 'locking' parameter used to limit chain extensibility under large deformation, and bulk modulus, respectively. Stress can be derived as:

$$\sigma = \frac{\mu J_m}{J_m - I_1 + 3} B + K(J - 1)I \tag{29}$$

For incompressible, uniaxial tension, the stress becomes:

$$\sigma_{11} = \sigma = (\lambda^2 - \frac{1}{\lambda})(\frac{\mu J_m}{J_m - I_1 + 3})$$

$$\sigma_{Eng} = \frac{\sigma}{\lambda} = (\lambda - \frac{1}{\lambda^2})(\frac{\mu J_m}{J_m - I_1 + 3}) \tag{30}$$

where $I_1 = \lambda^2 + \frac{2}{\lambda}$. Note that, if $J_m \to inf$, the solution is identical to the neo-Hookean form. In general, the Gent model is advantageous for its simple nature and high accuracy: specifically that it is a two-parameter model (excluding bulk modulus) with one parameter being shear modulus itself.

3.2.5 Hyperelastic Model Comparison

Overall, most of these models are effective for certain applications and over specific stretch ranges. However, a comparison for the predictive capabilities of each model is shown below in Table 3.1 to give a better sense of model robustness and efficacy. The number of material parameters required to fully define each model given an incompressible material is also presented in Table 3.1. While the constants obtained and material parameters vary for each model and often have arbitrary meanings, specific parameters such as shear modulus, μ, can be directly compared across models. From equation 2 above, elastic modulus can be calculated for those hyperelastic models in which shear modulus is a parameter.

Table 3.1. Overall Predictive Capabilities of Select Hyperelastic Models[17]

Hyperelastic Model	R^2-Prediction	Material Parameters
Neo-Hookean	0.794	1
Arruda-Boyce	0.973	2
Mooney-Rivlin	0.843	2
Yeoh (N=3)	0.980	3
Ogden (N=3)	0.998	6
Gent	0.972	2

3.3 Mechanical Oscillator

Numerous methods and instruments have been developed to measure the properties of materials. While each method ranges in complexity, they fall into a few primary categories: static and dynamic methods. Static methods include tensile tests such as uniaxial stress or uniaxial strain tests and flexural testing methods, although this is only ideal for brittle materials. Dynamic methods include resonance and impact excitation methods that use natural frequencies to

calculate elastic modulus. Techniques include continuously vibrating beams at select frequencies to sweep for resonance or by striking a beam and recording the sound to determine frequency. However, these methods themselves are also not optimal for elastic materials. Furthermore, these well-developed methods tend to involve expensive machinery that is not widely accessible for use. Even the most common tensile testing instruments, such as Instron machines, for example, are very expensive and typically only available to larger institutions.

A mechanical oscillator, however, is a low-cost, accessible, and straightforward method to determine the elastic modulus of elastic materials. Mechanical oscillators involve a cyclic conversion between potential energy stored in deformed elastic materials and kinetic energy from a mass in motion. In this study, the potential of a mechanical oscillator for characterizing rubber-like silicone elastomers is examined. The findings could provide another alternative to understanding the stress-strain relationship of elastic and hyperelastic materials.

Much like other dynamic methods, the frequency of cyclic motion from the mechanical oscillator can be used to estimate elastic modulus. The governing equation for these systems vary based on their configuration. In general, however, the constitutive equation will include an inertial term dependent on acceleration, a restoring force dependent on material stiffness, and a damping term dependent on strain rate. The magnitude of this damping reflects the material damping coefficient, and assumes inefficiencies between the periodic conversion of kinetic and potential energy is the result of the material properties and behavior instead of physical aspects of the oscillator configuration such as friction or air resistance. The validity of this assumption will later be discussed retrospectively as well.

3.3.1 Horizontal Configuration

For the purpose of this study, a horizontal mechanical oscillator configuration was designed to meet two primary criteria: a straightforward set-up in which data can easily be recorded without expensive machinery and the material always acting in tension. A biaxial configuration, for example, would make it difficult to effectively track mass position and out-of-plane forces could create motion that would require multiple, synchronized cameras to track. This would complicate the method in a way that would defeat the purpose of the mechanical oscillator as a simple method to estimate material properties. The chosen horizontal configuration, shown in Figure 3.3 and Figure 3.4 below, was used to satisfy both of these conditions.

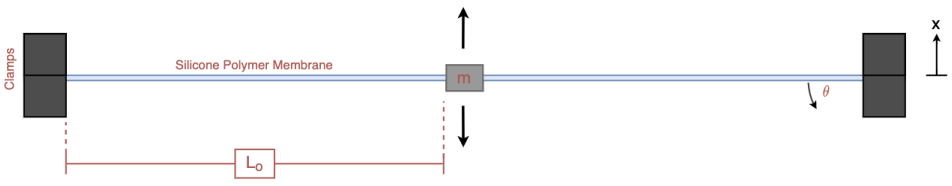

Figure 3.3. Side view of horizontal mechanical oscillator system

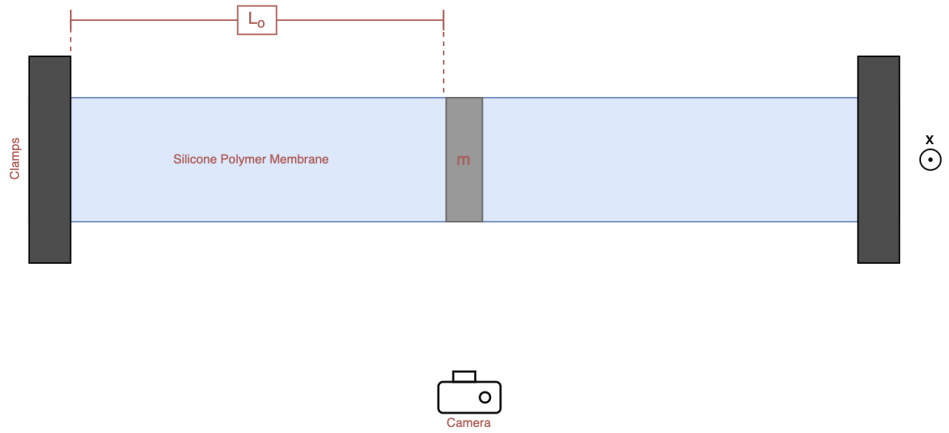

Figure 3.4. Top view of horizontal mechanical oscillator system

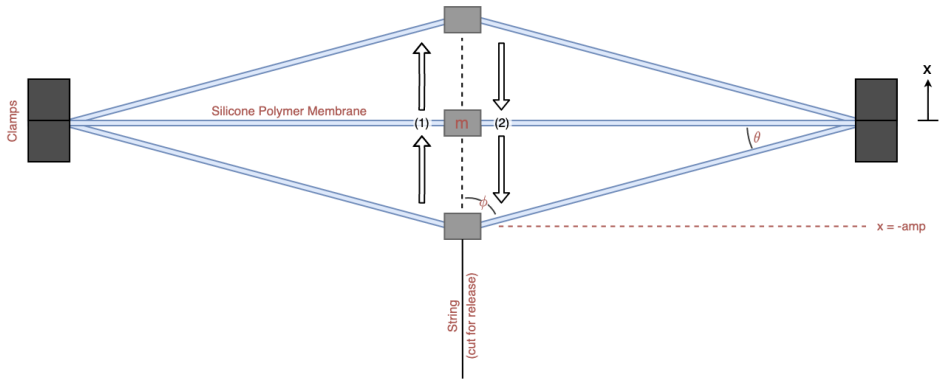

Figure 3.5. Deformed state and motion of horizontal mechanical oscillator system

$$F = m\frac{d^2x}{dt^2} \tag{31}$$

$$F = F(\varepsilon) + F(\eta, \frac{d\varepsilon}{dt}) + F(g) \tag{32}$$

$$m\frac{d^2x}{dt^2} = -2EA_o sin(\theta)(\frac{(x^2+L_i^2)^{1/2} - L_o}{L_o}) - 2\eta A_o(\frac{x}{(x^2+L_i^2)^{1/2} L_0})\frac{dx}{dt}cos(\phi) - mg \tag{33}$$

$$\theta = tan^{-1}(\frac{x}{L_i}) \text{ and } \phi = tan^{-1}(\frac{L_i}{x})$$

The basic law governing the horizontal mechanical oscillator is Newton's Law (31). From the figure and knowledge of the materials being used, there are three influences on the oscillating mass: a force from the polymer membrane in tension that is dependent on strain, a viscous damping force dependent on a material damping constant and strain rate, and a constant force due to gravity. In these equations, ε is strain, η is a material property describing viscous damping, g is acceleration due to gravity, m is mass, E is elastic modulus, A_o is membrane cross-sectional area, L_i is initial unstretched membrane length, and L_o is initial horizontal membrane length in the mechanical oscillator with an applied pre-stretch. Since the oscillator mass is much larger than the membrane mass, the configuration can be idealized as a spring-mass-damper system and the vibrational mechanics and wave propagations through the membranes are negligible.

For the horizontal oscillator configuration chosen in this experiment, the governing equation is shown in Equation 33, and derived from the schematic. The force exerted on the mass due to material stretching is equivalent to the product of the elastic modulus for a given strain and cross-sectional area. The non-vertical forces from the membranes offset, so only forces in the vertical direction dictate the movement. Due to the range of the tangent inverse, $-\frac{\pi}{2} < \theta < \frac{\pi}{2}$ and $-1 < sin(\theta) < 1$, so the force will act upwards when $x < 0$ and downwards when $x > 0$. Furthermore, the force due to viscous damping will oppose the velocity, with no direct dependence on position. Thus, with the same range of ϕ as for θ, $0 < cos(\phi) \leq 1$ and the direction of this force contribution depends entirely on the direction of velocity. These angles are also depicted in Figure 3.5. Lastly, there is a constant gravitational force directed downwards.

The following system of differential equations is solved for position and velocity. Taking $x_1 = x$ and $x_2 = x'$, the governing equations above become:

$$x' = x_2$$

$$x_2' = (-2EA_o sin(tan^{-1}(\frac{x_1}{L_o}))(\frac{(x_1^2+L_i^2)^{1/2}-L_o}{L_o}) - 2\eta A_o x_2 cos(tan^{-1}(\frac{L_o}{x_1}))(\frac{x_1}{(x_1^2+L_i^2)^{1/2}L_0}) - mg)/m$$

Mass, amplitude, initial length, and pre-stretched length are all prescribed constants. Elastic modulus and the viscous damping coefficient are estimated and ultimately determined through curve-fitting on MATLAB. Note that, given the small strain ranges present in the set-up, we assume linear elasticity so elastic modulus is constant. Multiple tests are required with varying pre-stretch to investigate and estimate the elastic modulus at another strain range. The initial conditions $x(0) = -amp$ and $x'(0) = 0$ are applied to an ordinary differential equation solver (ode45) in MATLAB and predicted position and velocity as a function of time can be plotted. These solutions can ultimately be compared to experimental data using MATLAB video tracking for position (x_1), which can subsequently be used to determine velocity, x_2. Unknown constants, such as η, can be estimated by comparing the curves and seeing which values fit the experimental results to computational predictions.

3.3.2 Vertical Configuration

In addition to the horizontal configuration outlined above, a vertical oscillator configuration is also tested. A vertical configuration is chosen in order to test material properties at higher strain rates. While the small angles from oscillation in the horizontal configuration limit strain rates, the vertical oscillator is used to achieve high strain rates as all movement of the mass is in line with the membrane. The strain rates achieved through this configuration can far exceed the strain rates from uniaxial testing instruments, and will be used to estimate the effect of viscous damping effect at higher strain rates. The set-up is outlined in Figure 3.6 below.

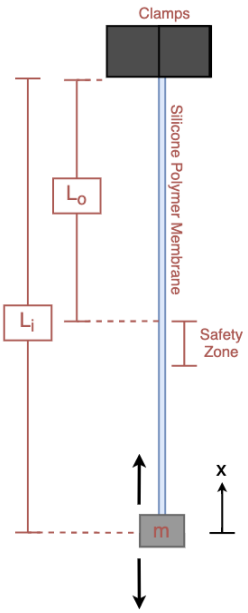

Figure 3.6. Schematic of vertical mechanical oscillator system

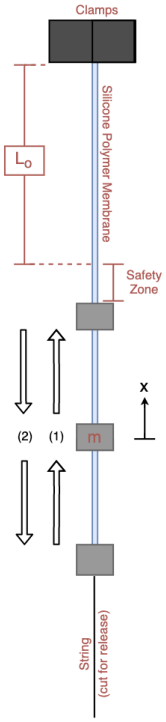

Figure 3.7. Deforemed state and motion of vertical mechanical oscillator

In order to remain in tension throughout movement, the mass is oscillated such that it will always remain well below its initial, unstretch length, L_o. The governing equation for this system is derived in a similar manner to the horizontal system, and the solution is shown in equation 34.

$$m\frac{d^2x}{dt^2} = EA_o\left(\frac{L_i - x - L_o}{L_o}\right) - \eta\frac{dx}{dt}\frac{1}{L_0} - mg \tag{34}$$

As the membrane undergoes large changes in stretch under this configuration, the initial resting stretch (L_i) and amplitude of oscillation is chosen based on uniaxial results for an approximately linear region of stress-strain. This assumption is approximately true at stretches ranging between $1.5 < \lambda < 2.5$. Thus, elastic modulus, E, can be estimated as a constant–the validity of this assumption will be determined by the ability to predict and replicate motion computationally. The mass is tracked by a slow-motion iPhone camera and the system is solved on MATLAB as outlined in the previous section.

3.3.3 Mechanical Oscillator Testing Approach

Ultimately, experimental data can be used to estimate the force exerted on the mass by the sample over a range of strain values. For the horizontal configuration, a number of repeated tests need to be taken with varying initial strain lengths to estimate the elastic modulus at any given strain. Although these strain values are less extensive than the full range obtained by a uniaxial test, a stress-strain relationship can be established for this area. Increasing and decreasing masses, pre-stretch, and initial excitation amplitude will change the range of strains being tested, and a stress-strain curve can be built over a greater range of strains. Results obtained via this method can be fit with the hyperelastic models mentioned in the previous section and compared to the results from uniaxial testing to determine the validity and potential of this method as a low-cost and accessible alternative to sophisticated uniaxial testing instruments for determining the material properties of hyperelastic materials. The decay in oscillation amplitudes can be used to estimate a damping coefficient for the material as well.

Furthermore, the vertical configuration will also be used to test samples at very high strain rates: notably higher than the uniaxial testing instrument. This test can be used to examine the viscous damping effect of the material at high strain rates, and determine if these effects are noticeable at the obtained strain rates. Ideally, the viscous damping coefficient can be calculated from this method–confirming the results obtained from the horizontal configuration at even higher strain rates.

4.0 Materials and Methods

4.1 Silicone Polymer Synthesization

Silicone polymer membranes were synthesized using MoldStar Series: Platinum Silicone Rubber Part A, Mold Star Series 16 Fast: Platinum Silicone Rubber Part B, Mold Star Series 15 Slow: Platinum Silicone Rubber Part B, and BJB Enterprises TC-5005 Part C. These will be referenced as Part A, Part B fast, Part B slow, and Part C, respectively.

Proper amounts of each part are measured to contain equal mass of Part A as Part B fast and slow, and Part C is variable as a percentage of the total amount (Part A, Part B fast, and Part B

slow). In general, relatively large amounts of all parts were used to minimize error and minor deviations in net weight between parts. Equal parts A and B (fast + slow) were taken to ensure an ideal ratio of polymer to cross-linkers in the mixture, and Part C was added based on the desired material stiffness and application. All three parts were mixed thoroughly, degassed at around -0.85atm for five minutes to remove air bubbles. It is important to note that, adding no Part C to the mixture makes degassing very difficult and can lead to air bubbles in cured membranes, while adding too much Part C (over 100%) can lead to very soft membranes that tear easily.

A leveling device was calibrated and set to a height at least 300μm above the ultimate desired membrane thickness, usually around 750μm. Liquid silicone was then poured onto a flat, clean glass pane and the leveling device was steadily pulled across the glass and set aside. Liquid silicone was then left to cure at room temperature overnight. Desired membrane samples were laser-cut and carefully removed from the glass.

4.2 Compliant Membrane Foil Construction

Constructing compliant membrane foils was a careful process with each step requiring focus to maintain a clean, uniform hydrodynamic foil. A rectangle with dimensions 150mm x 425mm was laser-cut but not removed from the glass. Instead the surrounding excess membrane material was removed. Four wood planks roughly 1” wide and longer than the rectangle were obtained, and each marked with a line down the center. A thin, uniform layer of silicone adhesive glue (Sil-Poxy Silicone Rubber Adhesive, or Gorilla 100% Silicone Clear Sealant) was added to one side of one of the planks. A paper towel was aligned along the edge of the membrane rectangle, and the wood plank was glued onto the membrane so that half of the plank was on the membrane and the other half on the paper towel. Excess paper was cut off. The process was repeated for the other side, weights were placed on top of the planks, and the glue was let to dry for two hours. The exact width of the membrane between the planks was measured and recorded.

Wood planks were then removed from the glass with the membrane, using a thin, metal spatula to help lift the membrane from the glass when necessary. Glue was carefully added to any areas where the membrane was not completely attached to the plank. Once the membrane was separated from the glass, it was flipped over and the other two wood planks were glued to the membrane and planks on the other side, sandwiching the membrane between each pair of planks. The wood planks were glued to a stretching rig, and fixed in parallel at a desired pre-stretch, usually 10 or 15%.

Two thin steel frames were obtained to serve as the frame of the foil. Gorilla Epoxy Clear glue was mixed and applied in a thin layer around one side of each frame, and let harden for 15 minutes. All-purpose Krazy Glue was added onto the hardened epoxy on one frame, and carefully placed glue-side down in the center of the stretched membrane. The frame was lightly and repeatedly pressed down on all sides, and a thin layer of Krazy Glue was applied around the

outside of the frame. The glue was let to dry for 10 minutes, the stretching rig was flipped over, and the process was repeated on the other side with the second steel frame. The finished foil was the cut from the stretching rig and excess membrane material was removed with the laser cutter. An example of a finished foil is shown below in Figure 4.1 below.

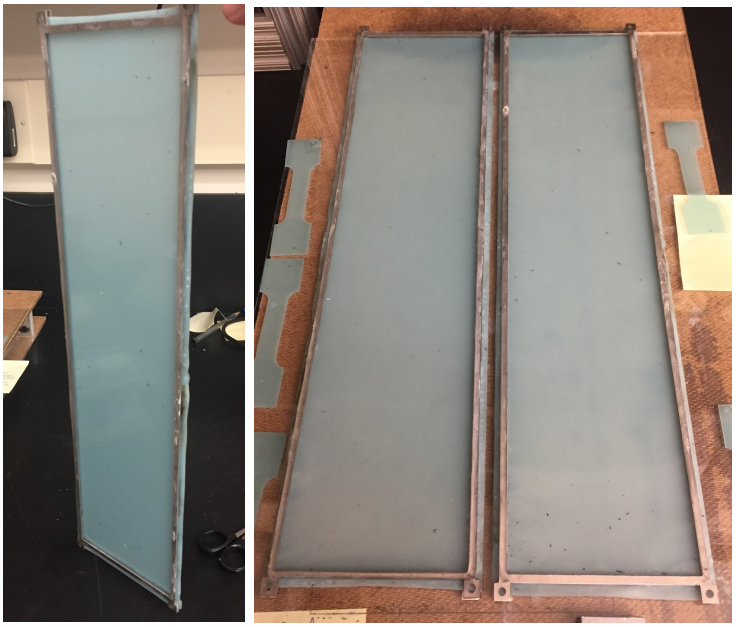

Figure 4.1. Compliant membrane hydrodynamic foil

4.3 Uniaxial Testing

Dogbone-shaped samples were used for uniaxial testing (Figure 4.2). Sample thickness was measured and recorded using calipers, and a rapid manual pre-stretching was applied roughly 5 times to each sample to minimize the Mullins effect. Samples let rest for a few hours, and were then carefully placed between two plates on either side using thick double-sided tape to hold the sample in place. Samples were fastened into an Instron uniaxial testing machine, and force-displacement measurements were taken over a wide range of strains and strain rates. Data were converted into stress and strain separately based on sample dimensions.

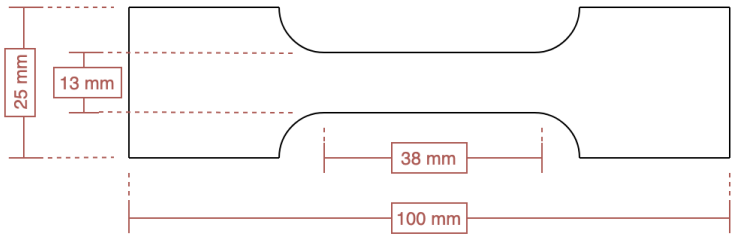

Figure 4.2. Uniaxial testing 'dogbone' sample

4.4 Mechanical Oscillator Testing Instrument

A single long rectangular sample was used with the setup outlined in Figure 3.3 and Figure 3.4. Masses were cut from a 1 mm thick sheet of lead of desired width and length equal to the rectangle sample width. Thin, lead masses were fastened using tape to the center of the rectangular sample on either side for even weight distribution and to minimize torque effects. The precise length of each side was measured with a caliper. A cotton string, at least 20cm long, was securely taped to the center of the bottom mass: this is an integral aspect of ultimately being able to excite the system in a consistent and controlled manner.

Samples were then aligned and secured on either side to the testing rig, using binder clips to securely hold end plates. The desired sample length (including pre-stretch) was applied with the adjustable end of the rig. The zero displacement of the sample was measured and recorded. An iPhone camera was held in place level with the sample and set to record with the slow-motion setting. Samples were tested by pulling the cotton string directly downwards to the desired amplitude, swiftly cutting the string with sharp scissors to minimize unwanted forces, and recording the mass oscillating up and down (Figures 3.5 and 3.7). Video recordings were post-processed on MATLAB, with the position of the mass being tracked throughout the test.

5.0 Results and Discussion

5.1 Uniaxial Studies

In order to use hyperelastic models to characterize the material, the material behavior must be independent of the rate of testing. A series of tests was conducted in order to determine these effects. First, samples were stretched statically (at very low strain rates) until failure to determine their failure points and establish an operating range for future tests. Thus, future experiments that required samples to be tested multiple times stayed well below these failure strains, so no plastic deformation occurred in the samples. These results are plotted in Figure 5.1. Recall that, from the procedure, all samples undergo a manual pre-stretching before uniaxial testing. This is to eliminate the Mullins effect present in some rubbers experiencing strains for the first time. The phenomena is shown in Figure 5.2, in which the sample did not undergo manual stretching before testing.

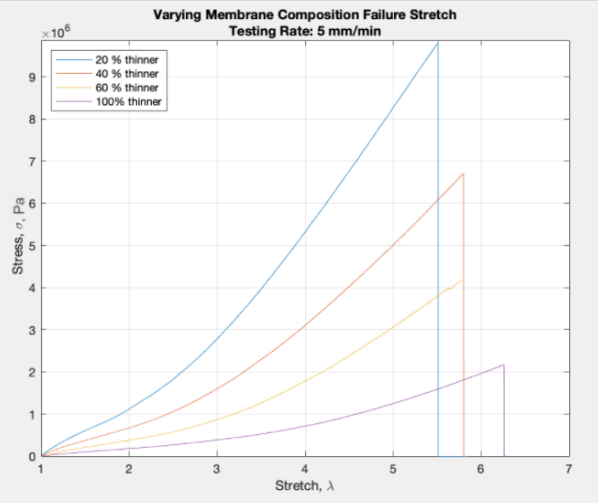

Figure 5.1. Membrane testing until failure

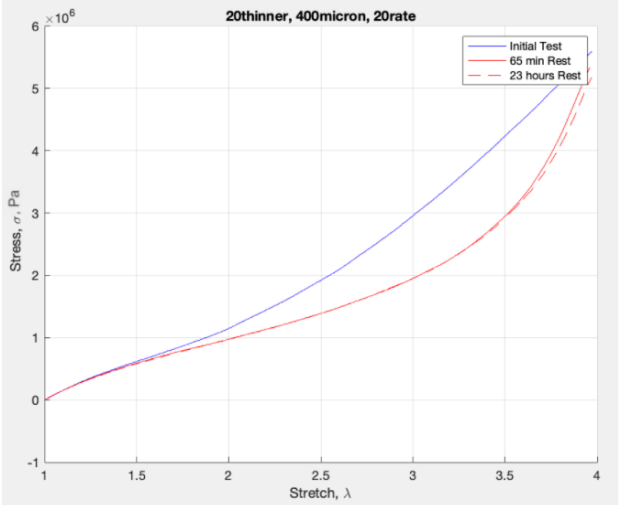

Figure 5.2. Mullins effect in virgin sample

Even though all silicone membranes can stretch well beyond 4 times ($\lambda = 5$) their initial length, future testing was conducted over the range $1 < \lambda < 4$ to avoid any permanent deformation or changes in material molecular structure for even the stiffest silicone membranes.

The permanent set phenomena described in Section 3.1 also needed to be addressed. After returning samples to original length after each test ($\lambda = 1$), samples did not go back to their initial taught state, and, instead, a noticeable elongation between 0-2mm was typical. Although this permanent set was no more than 5% elongation, it was still necessary to take into consideration. Thus, a wait time between repeated testing of the same sample needed to be established to ensure accurate data and consistent results. Samples were tested under various wait times (Figure 5.3) and data were fit on MATLAB with a smooth, continuous, differentiable spline using the built-in MATLAB spline fitting 'spaps' function and applying appropriate tolerance to ignore raw data noise (Figure 5.4). While the raw data were very consistent regardless of wait time, infinitesimal elastic modulus was plotted over stretch by differentiating the spline fits (Figure 5.5). In general, small changes in the stress-strain relationship can lead to large changes in elastic modulus since minor deviations propagate when taking derivatives. As can be seen in Figure 5.6, which shows the values of elastic modulus at the material initial and final stretch, elastic modulus does actually increase slightly with longer wait times. Note that the same analysis was conducted with silicone polymers containing only 50% thinner fraction, which yielded similar results with a less significant permanent set. A conservative approach was taken by establishing a 40 minute wait time for testing all samples to guarantee material recovery for the softest membranes and minimize the permanent set phenomena.

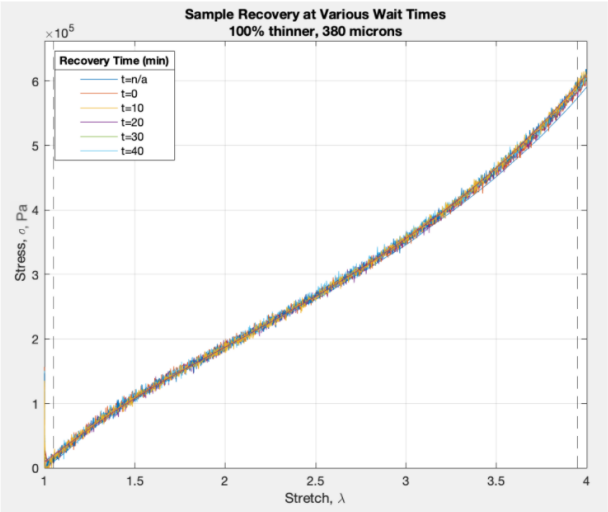

Figure 5.3. Uniaxial data with increased wait time

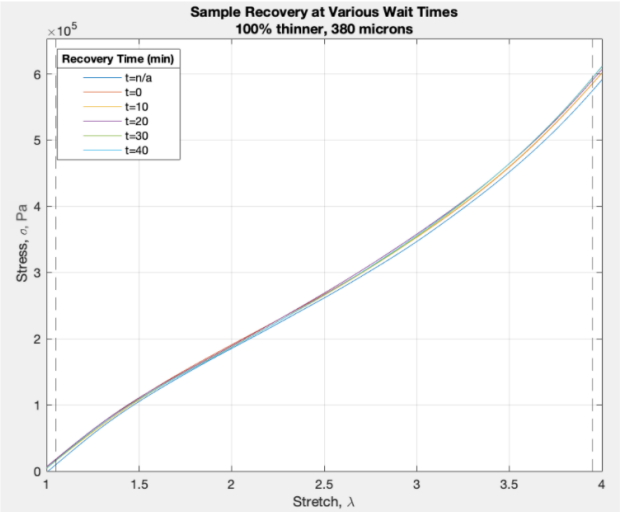

Figure 5.4. Smooth spline fit for raw data

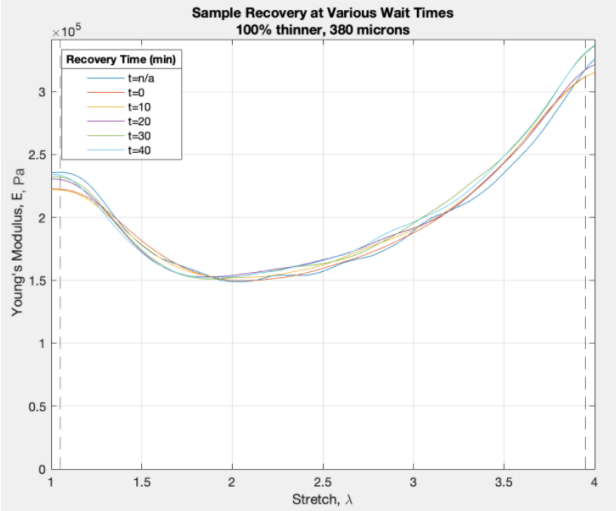

Figure 5.5. Infinitesimal elastic modulus

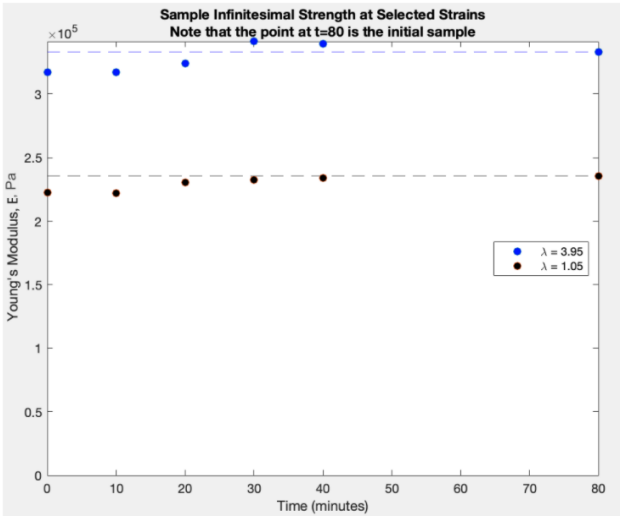

Figure 5.6. Elastic modulus at low and high stretch

In addition to short-term sample recovery, the material was also tested over extended time periods to determine whether loading had any long-term effects. This is especially important in the context of energy harvesting from hydrodynamic foils, which would need to function over longer periods of time. Samples were tested over a time span of three weeks and the results are shown in Figure 5.7 below. To estimate the elastic modulus over short stretch ranges ($1.1 \leq \lambda \leq 1.5$) the curves were fit with the Gent model and shear modulus was converted to elastic modulus using Equation 2 (Figure 5.8). Given the application of the material for energy harvesting, the chosen stretch range is appropriate as compliant membrane foil deformation will not exceed a semi-circular shape. Thus, in practice, the material will remain below $\lambda_{max} = \lambda_i \frac{\pi}{2}$ where λ_i is compliant foil pre-stretch (typically 1.05 or 1.1).

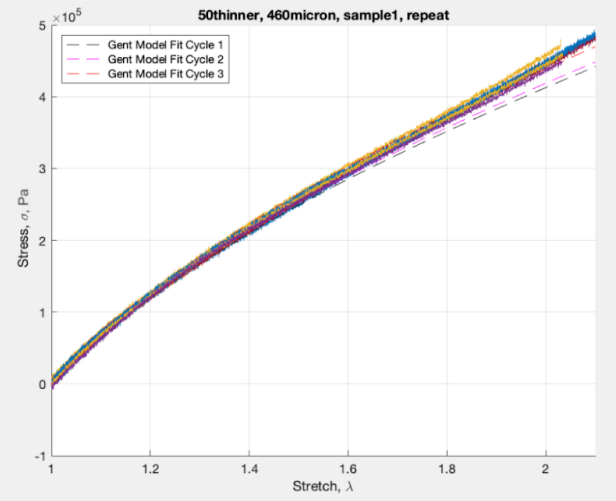

Figure 5.7. 50% thinner sample repeat testing 8 times across 3 weeks

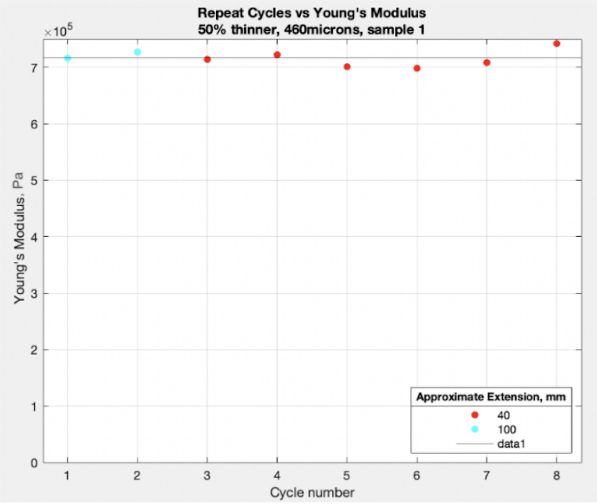

Figure 5.8. Young's Modulus from Gent model fits for each test

The results show that, even over longer periods of time, the material does not decrease in strength. In fact, each cycle was highly consistent and within 3% error. Most importantly, however, the cycles did not trend over time, and instead fluctuated naturally within a safe range. Although only data from one sample is shown above, a few different samples were tested which further confirmed these findings.

After establishing a wait time for repeat testing, samples were tested under a range of strain rates. Beginning with static analysis of 20mm/min, samples were tested repeatedly to 1600mm/min. This corresponds to a strain rate up to 0.67 s^{-1}. This maximum strain rate approaches the limit for the uniaxial testing machine. At least two samples with 20% thinner, 50% thinner, and 100% thinner were tested at strain rates of 20, 50, 100, 400, 800, and 1600 mm/min. Figures 5.9 and 5.10 below show the results for the highest and lowest strain rates for the stiffest (20% thinner) and softest (100% thinner) membrane samples.

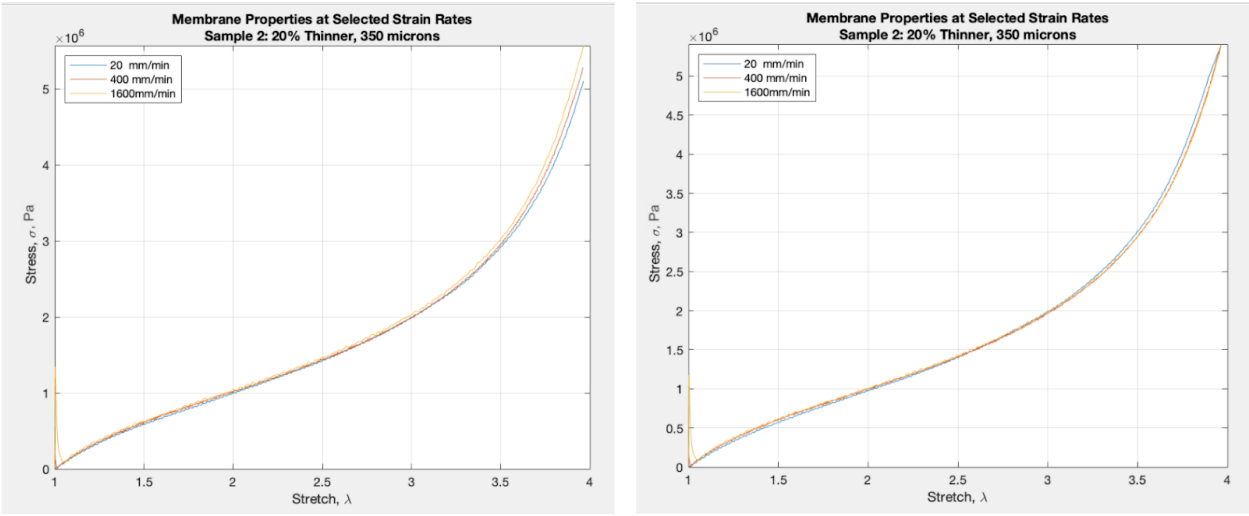

Figure 5.9. Uniaxial test results for 20% thinner silicone polymer at low and high strain rate

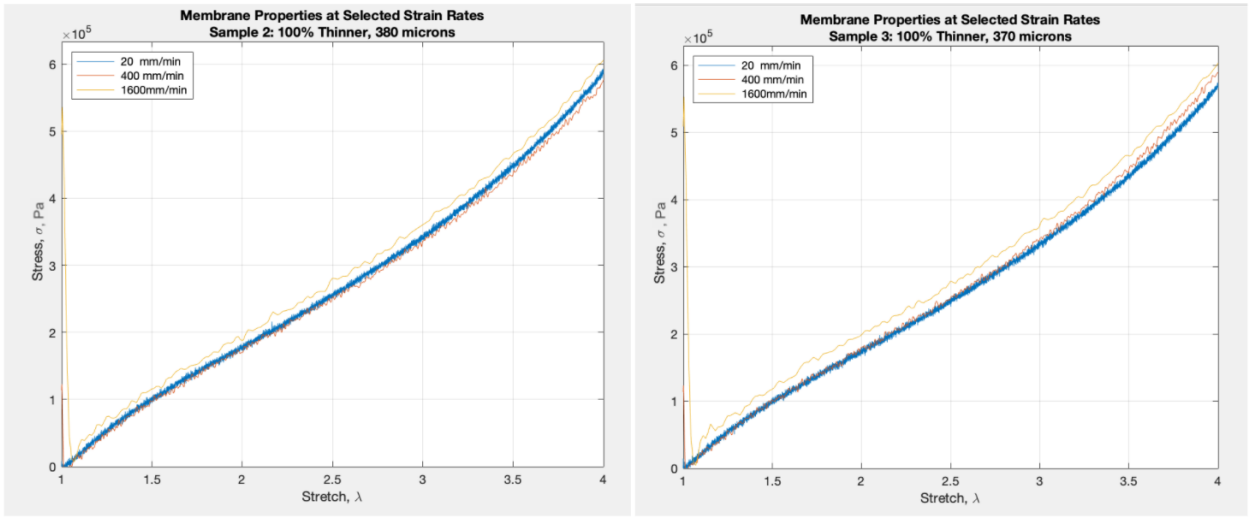

Figure 5.10. Uniaxial test results for 100% thinner silicone polymer at low and high strain rate

The results are consistent over the full range of strain rates, with none of the membrane compositions showing different stress-strain relations at increased strain rates. Although the material does exhibit some viscoelastic properties–as indicated by the presence of the permanent set–these effects are controlled for and minimized by establishing a wait time. Furthermore, as the material shows no dependence on strain rate, nonlinear hyperelastic constitutive models can be used to capture and define the material.

5.2 Fitting Hyperelastic Models

Utilizing the models and derivations outlined in section 3.2, each hyperelastic model can be fit to uniaxial data. In Table 5.1 below, the material parameters for each model are outlined for three different membrane sample compositions (20%, 50%, and 100% thinner). Note that all fit parameters for μ have units of MPa. Raw data for each composition was selected from multiple

membrane samples showing repeatability over many tests, to ensure that these samples were indeed indicative of the specific composition sample properties. Each model was fit on MATLAB over both the entire stretch range and over an optimal stretch range based on the model itself. The Arruda-Boyce, Yeoh, and Ogden models were fit over a select stretch range, starting from 30% strain since the mechanical oscillator tests were conducted above this pre-stretch value. The Neo-Hooke, Mooney-Rivlin, and Gent models were fit up until a select stretch value. In order to obtain realistic curve fits, specific model parameters were constrained based on values found in literature. Figure 5.11 (a-f) illustrates these curve fits with the raw data.

Table 5.1. Hyperelastic Model Parameters for Silicone Polymer Samples

Hyperelastic Model	**Strain Range**	**20% Thinner Membrane**	**50% Thinner Membrane**	**100% Thinner Membrane**
Neo-Hooke	$1 \leq \lambda \leq 4$	μ_1=0.809	μ_1=0.309	μ_1=0.127
	$1 \leq \lambda \leq 2$	μ_1=0.575	μ_1=0.240	μ_1=0.103
Arruda-Boyce	$1 \leq \lambda \leq 4$	μ=0.389, β=2.435	μ=0.212, β=3.182	μ=0.0959, β=3.559
	$1 \leq \lambda \leq 2.5$	μ=0.543, β=4.285	μ=0.218, β=3.322	μ=0.0941, β=3.379
Mooney-Rivlin	$1 \leq \lambda \leq 4$	μ_1=0.00136, μ_2=-1.64	μ_1=0.444, μ_2=-0.401	μ_1=0.172, μ_2=-0.132
	$1 \leq \lambda \leq 2.5$	μ_1=0.619, μ_2=-0.0708	μ_1=0.292, μ_2=-0.0854	μ_1=0.124, μ_2=-0.0333
Yeoh (N=3)	$1 \leq \lambda \leq 4$	C_{10}=4.07e^5 C_{20}=-1.92e^4, C_{30}=1049	C_{10}=1.20e^5 C_{20}=-3.96e^2, C_{30}=110	C_{10}=4.69e^4 C_{20}=4.86e^2, C_{30}=15.4
	$1 \leq \lambda \leq 2.5$	C_{10}=3.27e^5 C_{20}=-9.48e^3, C_{30}=740	C_{10}=1.13e^5 C_{20}=2.77e^2, C_{30}=101	C_{10}=4.78e^4 C_{20}=2.71e^2, C_{30}=31.6
Ogden (N=3)	$1 \leq \lambda \leq 4$	μ_1=0.674, α_1=1.813 μ_2=0.0001, α_2=8.444 μ_3=-0.001, α_3=0.000	μ_1=0.228, α_1=2.064 μ_2=0.00029, α_2=6.468 μ_3=-0.001, α_3=-0.180	μ_1=0.156, α_1=0.404 μ_2=0.0388, α_2=2.839 μ_3=-0.001, α_3=-0.298
	$1 \leq \lambda \leq 2.5$	μ_1=0.622, α_1=1.753 μ_2=0.0036, α_2=5.606 μ_3=-0.0321, α_3=-2.882	μ_1=0.286, α_1=1.320 μ_2=0.0284, α_2=3.562 μ_3=-0.001, α_3=-0.458	μ_1=0.235, α_1=1.813 μ_2=0.0001, α_2=8.444 μ_3=-0.001, α_3=0
Gent	$1 \leq \lambda \leq 4$	μ=0.465, J_m=22.1	μ=0.226, J_m=33.0	μ=0.100, J_m=41.0
	$1 \leq \lambda \leq 2.5$	μ=0.563, J_m=77.6	μ=0.230, J_m=36.7	μ=0.0993, J_m=39.1

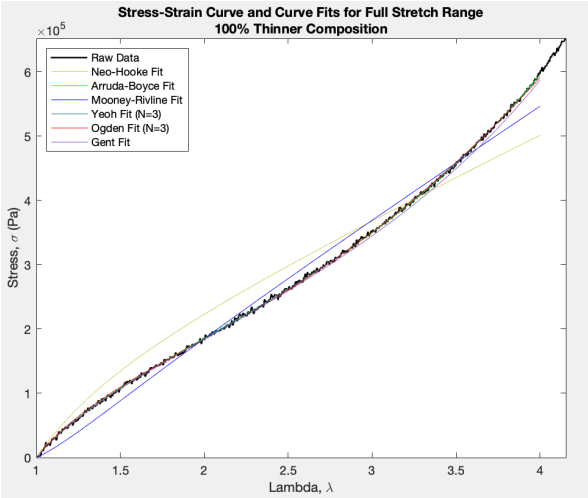
Stress-Strain Curve and Curve Fits for Full Stretch Range
100% Thinner Composition
×10^5
Raw Data
Neo-Hooke Fit
Arruda-Boyce Fit
Mooney-Rivline Fit
Yeoh Fit (N=3)
Ogden Fit (N=3)
Gent Fit
Stress, σ (Pa)
Lambda, λ

(a)

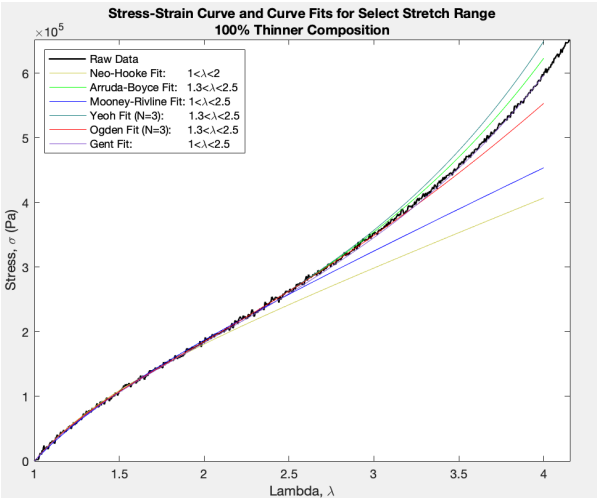
Stress-Strain Curve and Curve Fits for Select Stretch Range
100% Thinner Composition
×10^5
Raw Data
Neo-Hooke Fit: 1<λ<2
Arruda-Boyce Fit: 1.3<λ<2.5
Mooney-Rivline Fit: 1<λ<2.5
Yeoh Fit (N=3): 1.3<λ<2.5
Ogden Fit (N=3): 1.3<λ<2.5
Gent Fit: 1<λ<2.5
Stress, σ (Pa)
Lambda, λ

(b)

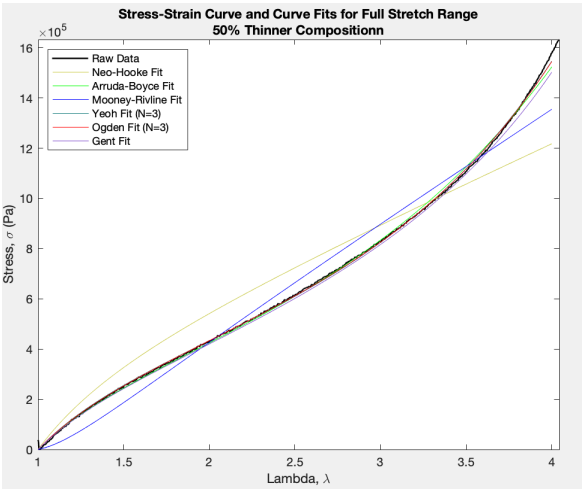
Stress-Strain Curve and Curve Fits for Full Stretch Range
50% Thinner Compositionn
×10^5
Raw Data
Neo-Hooke Fit
Arruda-Boyce Fit
Mooney-Rivline Fit
Yeoh Fit (N=3)
Ogden Fit (N=3)
Gent Fit
Stress, σ (Pa)
Lambda, λ

(c)

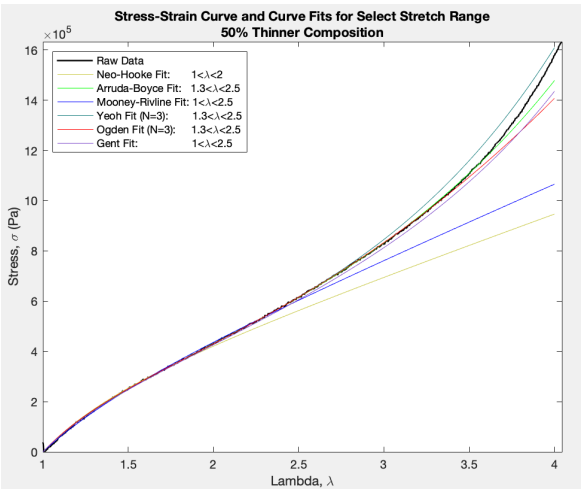
Stress-Strain Curve and Curve Fits for Select Stretch Range
50% Thinner Composition
×10^5
Raw Data
Neo-Hooke Fit: 1<λ<2
Arruda-Boyce Fit: 1.3<λ<2.5
Mooney-Rivline Fit: 1<λ<2.5
Yeoh Fit (N=3): 1.3<λ<2.5
Ogden Fit (N=3): 1.3<λ<2.5
Gent Fit: 1<λ<2.5
Stress, σ (Pa)
Lambda, λ

(d)

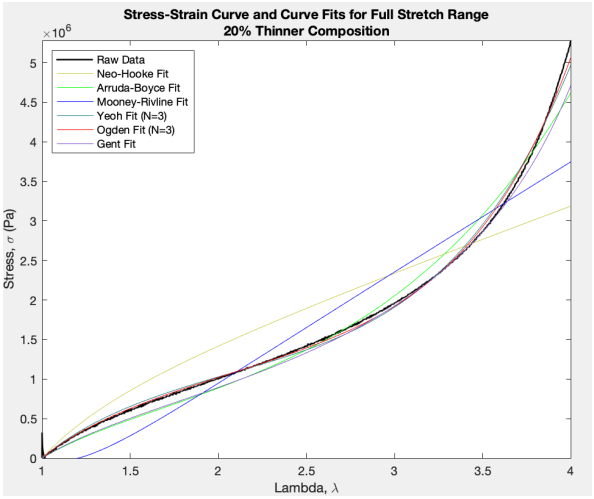
Stress-Strain Curve and Curve Fits for Full Stretch Range
20% Thinner Composition
×10^6
Raw Data
Neo-Hooke Fit
Arruda-Boyce Fit
Mooney-Rivline Fit
Yeoh Fit (N=3)
Ogden Fit (N=3)
Gent Fit
Stress, σ (Pa)
Lambda, λ

(e)

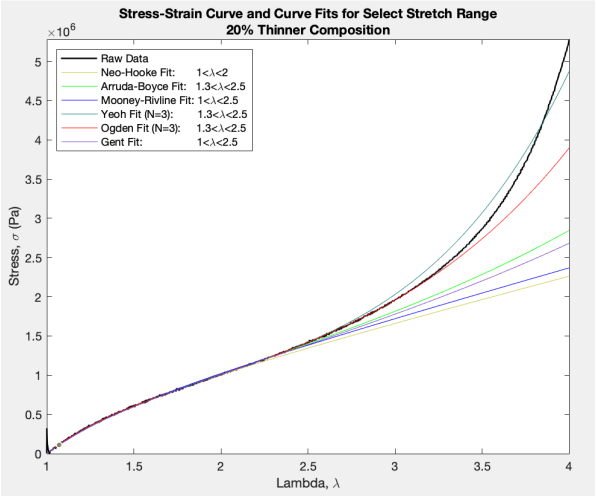
Stress-Strain Curve and Curve Fits for Select Stretch Range
20% Thinner Composition
×10^6
Raw Data
Neo-Hooke Fit: 1<λ<2
Arruda-Boyce Fit: 1.3<λ<2.5
Mooney-Rivline Fit: 1<λ<2.5
Yeoh Fit (N=3): 1.3<λ<2.5
Ogden Fit (N=3): 1.3<λ<2.5
Gent Fit: 1<λ<2.5
Stress, σ (Pa)
Lambda, λ

(f)

Figure 5.11. Hyperelastic model fits for membrane raw data over the full stretch range for (a) 100% thinner composition, (c) 50% thinner composition, (e) 20% thinner composition, and for select stretch ranges for (b) 100% thinner composition, (d) 50% thinner composition, (f) 20% thinner composition

A few noticeable features can be seen from these fits. Firstly, the Neo-Hooke and Mooney-Rivlin models are unable to capture the strain stiffening phenomena observed in the material. Thus, they are completely unable to model the material over the full range of data. However, both of these simple models fit the data accurately at lower stretch values, roughly until stretch reaches two. For the 50% and 100% thinner composition samples, the Arruda-Boyce, Yeoh, Ogden, and Gent model fit very well with the experimental data. For the 20% thinner composition sample, the models struggled to fit the data with the same precision as for the softer membranes, but the Yeoh and Ogden models still provided adequate fits. This can be attributed to drastic increase in elastic modulus at high stretch for the 20% thinner composition sample, for which the models struggled to accommodate the sharp increase in stress. For lower stretch ranges (up to 2.5), all models fit the data very well, with the exception of the Neo-Hooke model, which was only valid to a stretch of around two.

Based on the parameters obtained from the curve fits, Table 5.2 compares the elastic modulus values obtained from the model parameters. These values are obtained from shear modulus for each fit, and are trivially converted to elastic modulus from equation 2. Note that the values are primarily estimates assuming small strain.

Table 5.2. Elastic Modulus Determined from Hyperelastic Model Fits

Hyperelastic Model	Shear Modulus	Stretch Range	20% Thinner Membrane	50% Thinner Membrane	100% Thinner Membrane
Neo-Hooke	$\mu=\mu_1$	$1 \leq \lambda \leq 4$	2.43 MPa	0.928 MPa	0.382 MPa
		$1 \leq \lambda \leq 2$	1.72 MPa	0.721 MPa	0.310 MPa
Arruda-Boyce	$\mu=\mu_0$ (eqn 17)	$1 \leq \lambda \leq 4$	1.31 MPa	0.677 MPa	0.302 MPa
		$1 \leq \lambda \leq 2.5$	1.68 MPa	0.694 MPa	0.298 MPa
Mooney-Rivlin	$\mu=\mu_1+\mu_2$	$1 \leq \lambda \leq 4$	-0.834 MPa	0.130 MPa	0.119 MPa
		$1 \leq \lambda \leq 2.5$	1.65 MPa	0.620 MPa	0.271 MPa
Yeoh (N=3)	$\mu=2C_{10}$	$1 \leq \lambda \leq 4$	2.44 MPa	0.717 MPa	0.282 MPa
		$1 \leq \lambda \leq 2.5$	1.96 MPa	0.676 MPa	0.287 MPa
Ogden (N=3)	$\mu=\mu_1+\mu_2+\mu_3$	$1 \leq \lambda \leq 4$	2.02 MPa	0.681 MPa	0.501 MPa
		$1 \leq \lambda \leq 2.5$	1.78 MPa	0.940 MPa	0.818 MPa
Gent	$\mu=\mu$	$1 \leq \lambda \leq 4$	1.40 MPa	0.677 MPa	0.300 MPa
		$1 \leq \lambda \leq 2.5$	1.69 MPa	0.691 MPa	0.298 MPa

The values obtained from these fits are indicative of the accuracy of the fit itself. As observed earlier, the Neo-Hooke and Mooney-Rivlin fits are poor for large stretch ranges, and the elastic modulus is altered significantly when the model is fit over an appropriate range. Surprising was the difference in elastic modulus for the Ogden model between the overall and enhanced range fits. This is due to the fact that determining shear modulus from the Ogden model relies on three parameters, so small changes in each value propagate into large errors in the estimate for elastic modulus. The remaining three models were consistent for the 50% and 100% thinner composition samples despite the difference in stretch range used to fit the model, with discrepancies up to only 6%. These similar values validate the accuracy of the fit and efficacy of the model over both select stretch ranges and large ranges. Every model showed significant difference for the 20% thinner composition sample, since ignoring the drastic increase in stress at high stretches enabled fits to adjust precisely at lower stretches.

In general, the models yield similar results in estimating shear and elastic modulus. Only the Ogden model shows remarkably different elastic modulus estimates from the other models. Table 5.3 compares each obtained value from the enhanced range fit to the elastic modulus average from the Arruda-Boyce model. The Arruda-Boyce model is chosen for its high accuracy in fitting data over select strain ranges (Figure 5.11) and good stability due to its physical background. By contrast, the Ogden model fits the data very well but is only stable when the product of the model parameters is positive (in one case a_3=0, and subsequently elastic modulus estimate is not accurate).

Table 5.3. Error in Elastic Modulus between Arruda-Boyce and Individual Hyperelastic Models

Hyperelastic Model	20% Thinner Membrane	50% Thinner Membrane	100% Thinner Membrane
Arruda-Boyce (Estimate)	1.68 MPa	0.694 MPa	0.298 MPa
Neo-Hooke	2.38%	3.89%	4.03%
Mooney-Rivlin	1.79%	10.66%	9.06%
Yeoh (N=3)	16.67%	2.59%	3.69%
Ogden (N=3)	5.95%	35.45%	174.50%
Gent	0.60%	0.43%	0.00%

Although the Ogden model fits the data very well, the constants and parameters obtained from these fits do not translate to shear or elastic modulus. The Neo-Hooke and Mooney-Rivlin forms are both accurate for the stiffer membrane, but perform poorly relative to the other models for the 50% and 100% thinner composition membrane. The Yeoh model is ineffective for the 20% thinner composition membrane, but the best predictor for elastic modulus of softer membranes. Overall, the Arruda-Boyce and Gent models are consistent and accurate regardless of the

membrane composition. The Gent model was chosen to estimate elastic modulus as it is the most accurate model across each membrane composition.

5.3 Silicone Polymer Membrane Composition and Elasticity

As the silicone polymer membranes can be designed and optimized to obtain a desired stiffness, a wide range of thinner (0-120%) can be added to the mixture before curing. Thus, a general sense for elasticity of the desired membrane composition should be known. Thickness can be altered as well to ultimately fine-tune stiffness for hydrokinetic energy harvesting applications.

Figure 5.12 shows the relationship between membrane composition and shear modulus. Each data point is the average of three samples, each tested three times and fit with the Gent model to obtain a value for shear modulus. The tested samples were fit with the Gent model over an initial range up to stretch values of 1.5, given the application of the material as hydrokinetic foils. The error bars represent the maximum and minimum value obtained from any one fit.

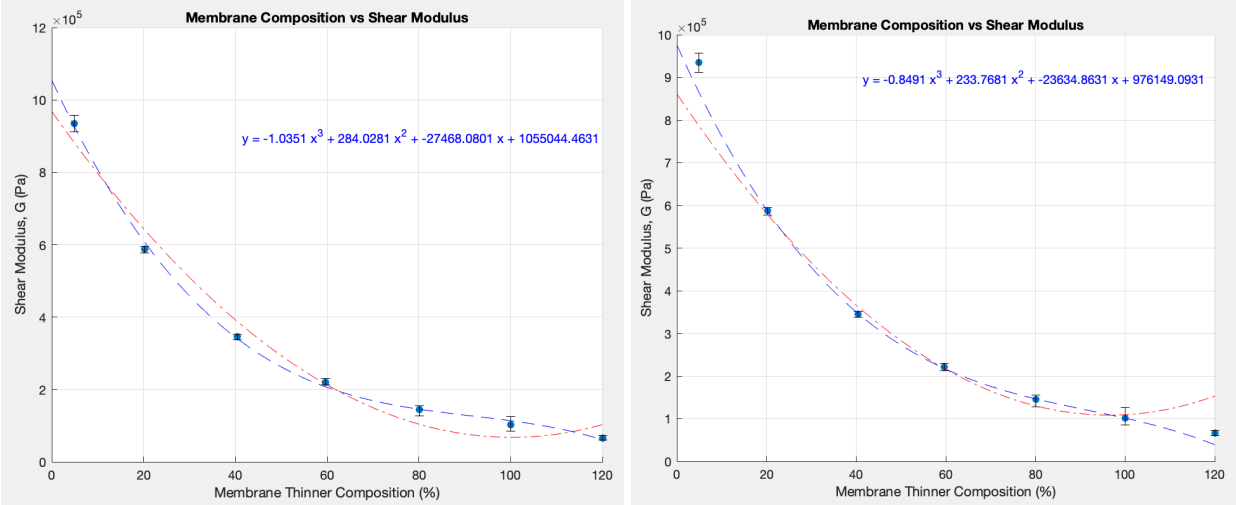

Figure 5.12. Shear modulus from the Gent model fit for varying membrane compositions. Data is fit with both Quadratic (red curve) and 3rd Order (blue curve) functions for the full data set (left plot) and excluding the extreme composition data points (right plot)

As the relationship between composition and shear modulus is clearly nonlinear, the points were initially fit with a quadratic function (red curve). However, the quadratic function predicts an increase in shear modulus at high compositions, which is intuitively nonsensical: an increase in thinner will always make the membrane softer, decreasing its shear modulus. Thus, the data were fit with a 3rd order function (blue curve) to ensure that the curve would always predict a decrease in shear modulus with increasing thinner composition.

Due to difficulties synthesizing membranes at low and high thinner compositions, caution needs to be taken when viewing the 5% thinner and 120% thinner compositions. The 5% thinner

composition is highly viscous and therefore difficult to degas. In turn, small air bubbles can form or remain in the sample during curing, leading to imperfections and slight inaccuracies. Conversely, the 120% thinner composition is an extremely soft and sticky membrane which also may be imprecise as samples deform even when removed from glass. While it is worthwhile to see that the obtained values lie where they are expected to, the precise values may not be accurate. As a result, the plot on the right shows the curves being fit for the middle five data points, excluding the extreme thinner compositions. The 3rd order function obtained from these data offers the best estimation of shear modulus for given thinner compositions from 0-100%.

5.4 Mechanical Oscillator - Horizontal Configuration

The potential of a mechanical oscillator to quantify the material modulus of elasticity and viscous damping coefficient was investigated through a series of experiments. The 'softest' membrane composition (100% thinner) was used in an attempt to bring out the viscous damping effect. For consistency of trials, all samples had an 80 mm width and 500 micron thickness. Figure 5.13 below shows sample data from video tracking. A smooth spline was fit to the data with 2% maximum amplitude tolerance for a smooth but accurate fit.

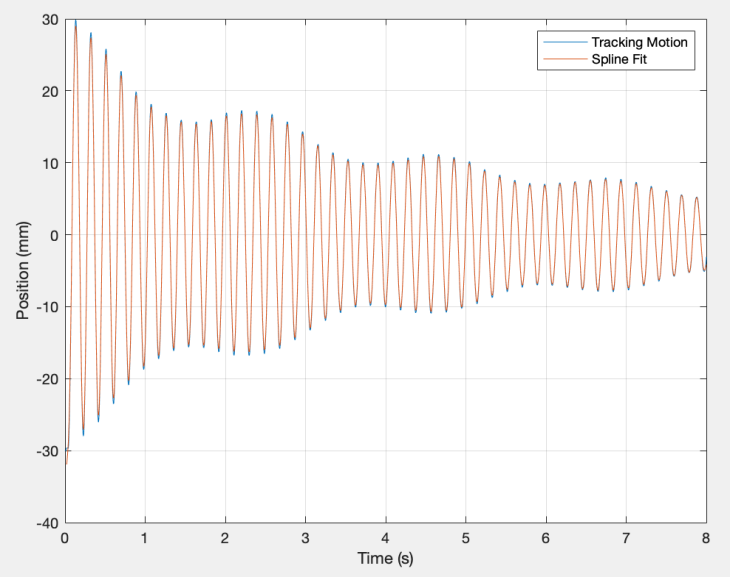

Figure 5.13. MATLAB Tracking Position for 1.3 pre-stretch, 30mm amplitude, 25.79g total mass, and 75mm initial length

A few notable phenomena can be seen from the MATLAB tracking results. As expected, there is a high periodicity of motion that is constant throughout the trial. The amplitude begins at a maximum and decreases over time. Initially, this decrease is rapid but at smaller amplitudes the decrease becomes minimal. This can be explained by some level of viscous damping, which will be discussed later. Furthermore, the effect of gravity is negligible: oscillations are not 'pulled' or skewed downwards due to the gravitational force, and instead the mass oscillates about the zero

displacement. This is due to the fact that the contributions from inertial force and elastic force dominate compared to the gravitational force since the mass is relatively small (equation 33). Finally, a secondary frequency can be observed from the sinusoidal behavior of the amplitude. This is the reflection of a torsional mode from imperfect testing. As the string-mass release is not always exactly perfect due to the nature of the experiment, a torsional mode can result. However, as experiments were repeated numerous times, it is evident that these secondary frequencies do not play a role in the primary frequency of oscillation and thus do not affect the estimation for elastic modulus.

Ultimately, tests for each selected pre-stretch value was performed at least three times, and each test lasted over seven seconds. Given the period length ranging from 0.15-0.23 seconds, each test contained over 30 oscillations. For each test, predicted results were fit to the governing equation of motion at least three times over a minimum of 5-10 periods. Figure 5.14 (a-i) shows examples of fit data over at least 10 oscillations for various pre-stretch conditions. For the most accurate and consistent results, the gravitational force was ignored. In Figure 5.14, the spline fit shows the experimentally obtained data and the predicted motion is derived from the ODE set up from Equation 33, with values for E and η adjusted to fit the experimental results.

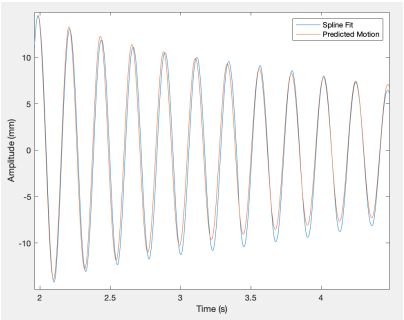

(a)

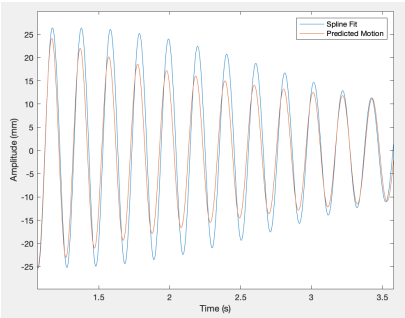

(b)

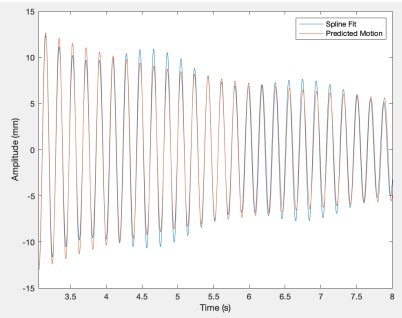

(c)

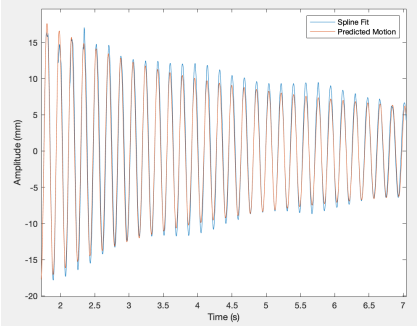

(d)

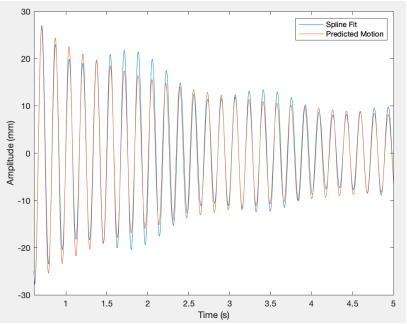

(e)

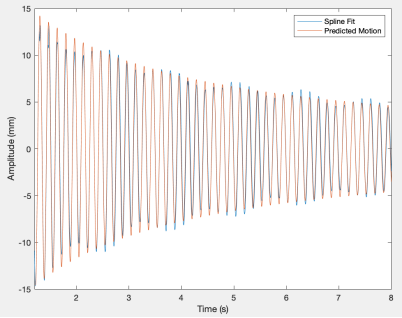

(f)

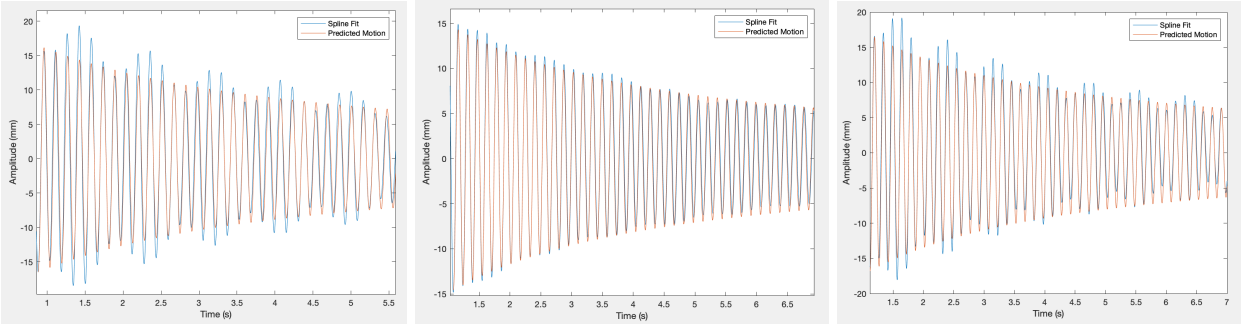

(g) *(h)* *(i)*

Figure 5.14. Experimental Tracking Result and Predicted Motion Fit for pre-stretch of (a) 1.1, (b) 1.2, (c) 1.3, (d) 1.4, (e) 1.5, (f) 1.6, (g) 1.7, (h) 1.8, and (i) 1.9 over select time intervals. Table 5.4 outlines the values obtained from these and similar fits

Despite the impact of secondary frequencies on the amplitude of oscillation, the clear trend downward is evidence of linear damping. Linear damping decreases amplitude by a factor of e^{-bt}, where $b = \frac{\eta}{2m}$ with viscous damping coefficient, η, and mass, m. Thus, with linear damping, decreases in amplitude are large initially and become gradual over time. Disregarding secondary frequencies, this trend is evident in our data. Thus, an estimation for viscous damping coefficient was determined by fitting curves over the general trend of the data, ignoring changes in amplitude caused by torsional modes. Figure 5.15 (a-e) shows estimates made based on experimentally obtained data. The estimates for viscous damping are obtained by fitting the curves to the form $y = Ae^{-\frac{\eta}{2m}t}cos(\frac{2\pi}{T}t)$, where amplitudes are estimated by $y = Ae^{-\frac{\eta}{2m}t}$. Due to the impact of secondary frequencies on amplitude, the values obtained for viscous damping coefficient have high uncertainty. As obtained values split the variations from secondary frequencies, uncertainty was determined by obtaining values that fell entirely within or outside of the oscillations over time.

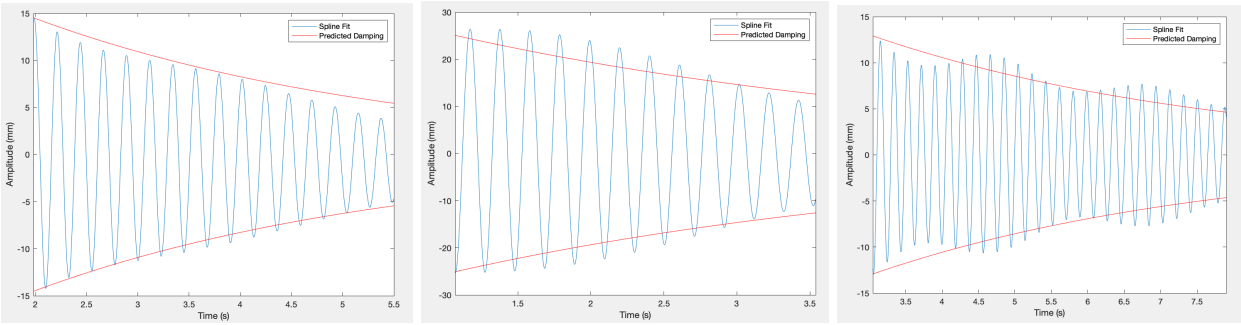

(a) *(b)* *(c)*

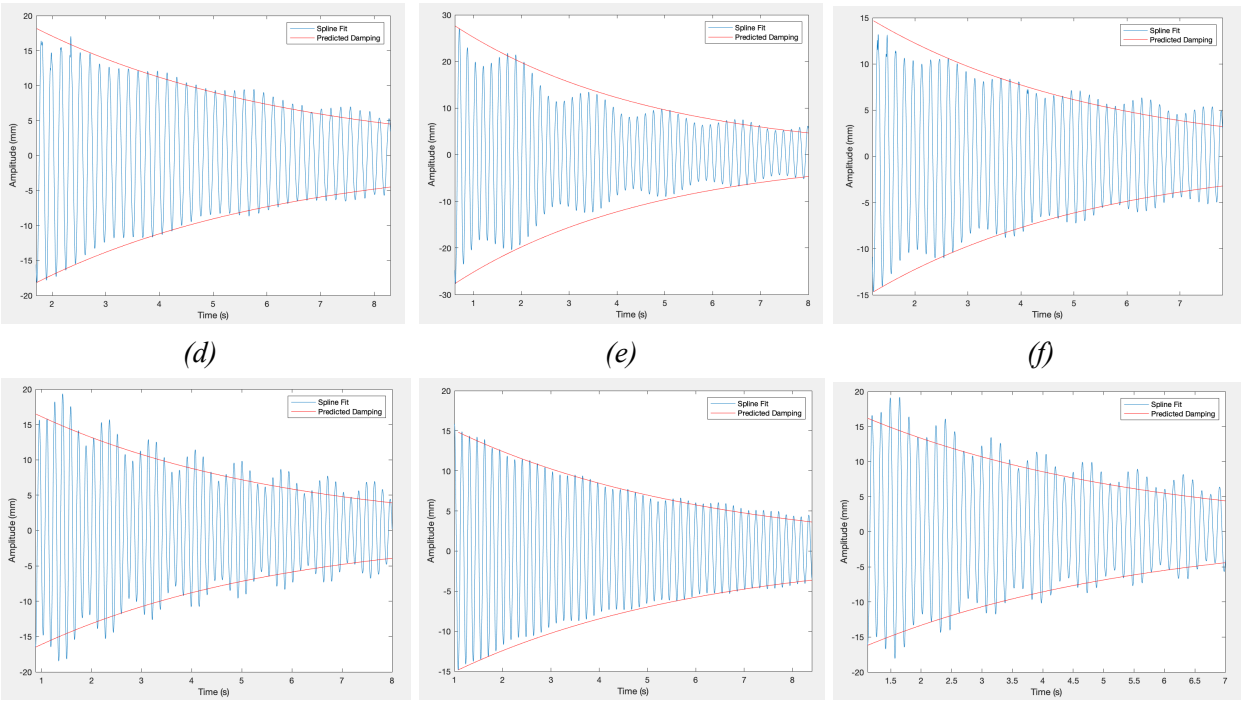

Figure 5.15. Viscous damping coefficient based on experimental data with pre-stretch (a) 1.1, (b) 1.2, (c) 1.3, (d) 1.4, (e) 1.5, (f) 1.6, (g) 1.7, (h) 1.8, and (i) 1.9 over select time intervals. Table 5.4 outlines the values obtained from these and similar fits

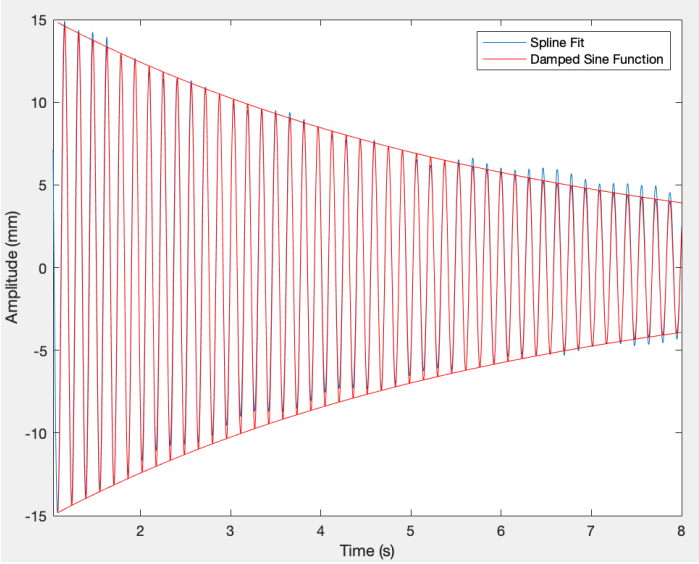

Figure 5.16. Comparison between experimental results and damped sine curve, as determined from the viscous damping coefficient and period of oscillation

After obtaining the oscillation period and a value for damping, the curves can be fit via another method: a damped sine function. These show very high alignment with the predicted motion as

well. As mentioned above, this function takes the form $y = Ae^{-\frac{\eta}{2m}t}cos(\frac{2\pi}{T}t)$, which is shown in Figure 5.15.

The following Table 5.4 shows the full results obtained from fitting the tracked oscillations (depicted in Figures 5.14). Estimates for modulus of elasticity, viscous damping coefficient, period, and strain rate are shown. The error for each condition is taken as a combination of the single minimum or maximum point from any one fit over more than 10 periods and uncertainties from measurements for mass and length. In general, the first few oscillations had marginally longer periods than the rest of the experiment, so these initial periods were largely ignored during post-processing. However, the period reached an equilibrium for later cycles in all valid experiments, and remained consistent for many oscillations. Thus, the data reflects these later cycles of motion, typically more than one second after release. Note that values for elastic modulus are scaled to reflect changes in cross-sectional area from stretching. After taking this into consideration, the values align very well.

Table 5.4. Elastic Modulus and Damping Coefficient based on Horizontal Oscillator Data

Stretch Range	Period (s)	Strain Rate (s^{-1})	Elastic Modulus (MPa)	Elastic Modulus Error (Min-Max)	Damping Coefficient (10^{-3} Ns/m)	Damping Uncertainty
1.10-1.19	0.226	1.68	0.224	0.215 - 0.234	15.20	±3.5
1.20-1.26	0.205	1.26	0.213	0.209 - 0.224	16.63	±2.5
1.30-1.36	0.189	1.27	0.190	0.180 - 0.198	7.62	±3.5
1.40-1.46	0.180	1.25	0.176	0.169 - 0.183	9.64	±2.0
1.50-1.59	0.170	2.16	0.170	0.162 - 0.174	16.55	±3.0
1.60-1.62	0.166	0.53	0.159	0.152 - 0.166	8.63	±3.0
1.70-1.72	0.161	0.52	0.152	0.145 - 0.159	11.71	±2.5
1.80-1.82	0.156	0.50	0.152	0.142 - 0.156	9.49	±1.5
1.90-1.92	0.149	0.50	0.153	0.145 - 0.159	12.14	±2.5

The results are as expected: a high initial elastic modulus followed by a decrease to a relatively constant elastic modulus. The period, regardless of amplitude of oscillation, was extremely consistent across each trial and showed no discernable variability. The strain rate was dependent on the range of stretch covered during each oscillation and the period. The strain rates are comparable or greater than those observed during uniaxial studies, which only covered ranges up to 0.67 s^{-1}.

Figure 5.17 compares the results obtained from the mechanical oscillator with estimations for elastic modulus from uniaxial tests. The uniaxial values are plotted over the full range of stretch.

The elastic modulus obtained from the mechanical oscillator results is also plotted with the diamond marker, and each point is labeled by the starting stretch. The results show that the horizontal oscillator can be used to predict the material elastic modulus for stretches from 1.1 to 1.9. Practical complications prevent from testing outside of this range for the horizontal mechanical oscillator, as the thin lead mass used in the experiment bends at high stretch. Given that the material must always be in tension, the minimum stretch tested is 1.1. All points are close to the uniaxial results, and within the uncertainty of the experiment.

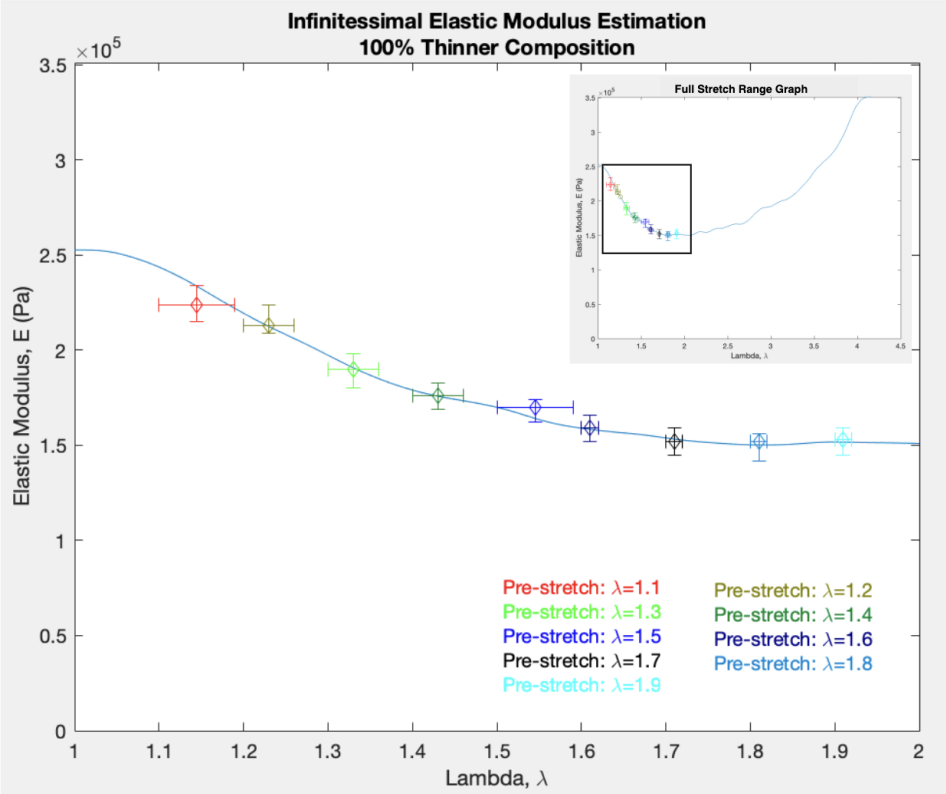

Figure 5.17. Comparison of Elastic Modulus Predicted from Oscillator (diamond markers) and Uniaxial Testing (blue line). Due to physical limitations with the mechanical oscillator method, the range of stretch for comparison is up to λ=2

Despite a conservative approach to error–which combines the range of values obtained from all tests and uncertainties associated with measurements–the error remains well within reason. The horizontal error bars represent the stretch range each test covered. Overall, these data show high repeatability and prove the consistency of the method. While results are repeatable, caution still needs to be taken when selecting data to report. Namely, poorly executed trials should be redone until proper. Poorly executed trials show very large variability in amplitudes between subsequent periods and can be distinguished both visually during testing and from tracking results. In these cases, secondary frequencies from torsional modes are so large that they will begin to impact the primary frequency of oscillations periodically, and are thus not able to be accurately modeled.

It should also be noted that, although not explicitly shown, there is also some uncertainty in the estimate for elastic modulus as determined by uniaxial testing. As the estimate relies on taking the derivative of a spline fit to noisy raw tensile data, the exact values depend largely on how well the spline fits the data without being affected by noise. The fit above was chosen to represent the 100% thinner composition since it aligned with multiple other uniaxial samples; still, although minor, the bumps in the curve are not actually representative of the material behavior. Increasing the tolerance of the spline fit would smooth these bumps, but sacrifice accuracy at low stretch ranges, which is not worthwhile in this case.

An advantage of the mechanical oscillator, besides being a low-tech method to estimate elastic modulus, is that it explicitly outputs a value for elastic modulus. By contrast, curves must be fit to uniaxial data and derived to estimate elastic modulus, in which spline fitting of noisy raw data can lead to error in estimating elastic modulus. Furthermore, the method enables use to quantify a viscous damping coefficient. The results (Table 5.4) for the damping coefficient are variable, but give a ballpark estimate between $8e^{-3}$ and $16e^{-3}$ Ns/m. The horizontal oscillator configuration enables torsional modes to cause secondary frequencies that impact period amplitude, making it difficult to obtain a viscous damping coefficient with higher confidence. Especially since oscillation data were taken from steady state–disregarding the first few oscillations–changes in amplitude are often small, so obtaining a value with high confidence is more difficult.

Despite estimating a coefficient for viscous damping, the values obtained do not necessarily represent material damping. Instead, damping could arise from air resistance, especially as the sheet of polymer used in the configuration is relatively wide and the change in the elastomer length caused by vibrations is small. For this horizontal configuration, the damping term is 3rd order for displacement during small oscillations, so the term becomes negligible when vibrations are small. This provides reason to believe that air resistance could play a factor in the observed damping from experimental results, as damping may be caused by a force not considered in our equation of motion. Regardless, a study of the oscillator conducted in a vacuum would provide a lot of insight into the contributions from both material properties and air resistance to damping.

Finally, some alternative methods for data interpretation can be explored in future directions. Experimental data can instead be compared with a linearized version of the equation of motion (Equation 33), and a relationship between stress in the material and natural frequency can be obtained. Much like the experiment above, repeated testing at different pre-stretch values can be conducted to obtain a range of values. Linearizing the equation of motion substantially reduces the complexity of the solution to the differential equation, however, this estimation would only hold true for small oscillations. These are especially hard to test at low pre-stretch values where larger oscillations are needed to properly excite the system.

5.5 Mechanical Oscillator - Vertical Configuration

The vertical oscillator configuration was tested to further study the damping coefficient, η. Due to the mass moving strictly in line with the membrane, high strain rates were obtained: above 4 s^{-1}. However, the data could not be accurately fit or predicted computationally due to the variable behavior of elastic modulus over large changes in stretch. Furthermore, the configuration is less robust than the horizontal configuration. Uncertainty associated with measurements for mass creates large variability in trying to estimate a value for tangent modulus. This is not surprising, as motion has a strong dependence on the gravitational force. As a result of both of these issues, the vertical configuration could not be used to obtain any useful estimates to characterize the material.

6.0 Conclusions

As populations across the globe look to address their carbon emissions, an emphasis is placed on renewable energy alternatives. Hydrokinetic energy extraction from hydrodynamic foils is a promising method for energy harvesting, especially in coastal regions. Within this field, compliant membrane foils have emerged as an area of interest, although the technology is still in a nascent stage. As a result, identifying an ideal material for these foils is critical in realizing the potential of these foils. This study looked to characterize the silicone polymer material being utilized for these foils.

Overall, uniaxial testing results showed no significant viscoelastic behavior. At strain rates present in energy harvesting applications, the material strength and loading will not change due to viscoelastic behavior. This is crucial, as viscoelastic behavior absorbs energy that would otherwise have increased power (and therefore foil efficiency). Additionally, the material did not show long-term changes in stress-strain relationship when being repeatedly tested over weeks. This is also critical given the material application–it should be able to maintain material integrity across month-long time spans.

To actually characterize the material, a few methods were employed. Uniaxial testing data were used to compare a variety of hyperelastic material models, and ultimately identify the Gent Model as the most effective model for our material. Estimates for shear modulus and elastic modulus were obtained from fitting uniaxial data with this model and used to identify the relationship between membrane thinner composition and desired elastic modulus. This relationship can be used to estimate stiffness of these silicone materials at any thinner composition between 5% and 100%. The initial addition of thinning liquid decreases the shear modulus greatly, so extra precaution needs to be taken if looking to obtain a shear modulus in this region. Thinner composition should never exceed 100%, as tear strength and material integrity become seriously compromised.

While hyperelastic models output a value indicative of material strength, actual strength of these nonlinear materials depends on the strain. Furthermore, as foils for energy harvesting, a pre-stretch can be applied to maintain tension in the foil and create a desired stiffness. Local material elastic modulus can be obtained by deriving for the slope of uniaxial data, however, the potential of a mechanical oscillator is also examined to estimate values for local elastic modulus. The results showed high agreement with uniaxial test data, and the mechanical oscillator also shows high repeatability. The oscillator very accurately calculates relative changes in elastic modulus at various stretch values ranging from 1.1 to 1.9. Additionally, the method provides an estimate for viscous damping coefficient, which gives a sense of the damping behavior of the material. The damping coefficient is a theoretical parameter that explains energy dissipation: at a maximum of $16e^{-3}$ Ns/m for the 100% thinner composition membrane. All other compositions will have a lower damping coefficient than this membrane, but precise values can be obtained by testing samples with this method. Further analysis, however, should be conducted to determine whether this phenomenon is actually the result of material properties or if it is instead influenced by air resistance.

In determining elastic modulus at a given stretch for nonlinear materials, measuring the slope of tensile data or using the mechanical oscillator is much more accurate than relying on a hyperelastic material model. The models tend to overestimate the local material strength, at least at small stretch ranges. The mechanical oscillator method is remarkable for its simplicity, very low cost, and accessibility. Furthermore, post-processing outputs desired values (E and η) directly. This method has implications for independent researchers and academics without access to uniaxial testing machines, which are usually only accessible to institutions and large corporations. The initial results are promising and the method should be investigated for more materials. Ultimately, the horizontal oscillator testing method developed in this study can be used to determine the elastic modulus at a desired strain and a viscous damping coefficient for hyperelastic or viscoelastic materials.

7.0 Acknowledgements

I would like to thank Professor Kenneth Breuer for his support, patience, and guidance throughout the project. I would also like to thank Varghese Mathai and Asimanshu Das for their advice and willingness to help me, especially given the increasingly independent nature of laboratory work in light of COVID-19. Additionally, I want to acknowledge Ben Lyons and Professor Chris Bull for their help in the Brown Design Workshop. Finally, I want to thank Professor Allan Bower for his insight and for taking the time to be a reader for my thesis.

8.0 References

[1] **Energy and the Environment Explained.** U.S. Energy Information Administration (2020)

[2] V. Mathai, G.A. Tzezana, K. Breuer, **Passive shape-morphing membranes enhance hydrokinetic energy extraction**, (Manuscript in preparation)
[3] A. Tiwari, M.D. Soucek, **Concise Encyclopedia of High Performance Silicones.** John Wiley & Sons (2014)
[4] P. Mazurek, S. Vudayagiri, A.L. Skov, **How to tailor flexible silicone elastomers with mechanical integrity : a tutorial review**, Chem Soc Rev, **48** (2019)
[5] F.B. Madsen, A.E. Daugaard, S. Hvilsted, A.L. Skov, **The Current state of silicone-based dielectric elastomer transducers.** Macromol Rapid Commun, 37 (2016), pp. 378-413
[6] L.-C. Tang, L. Zhao, F. Qiang, Q. Wu, L.-X. Gong, J.-P. Peng, **Mechanical properties of rubber nanocomposites containing carbon nanofillers Carbon-Based Nanofillers and Their Rubber Nanocomposites** (2019), pp. 367-423
[7] Y. Song, R. Yang, M. Du, X. Shi, Q. Zheng, **Rigid nanoparticles promote the softening of rubber phase in filled vulcanizates.** Polymer, 177 (2019), pp. 131-138
[8] R. Österlöf, H. Wentzel, L. Kari, **An efficient method for obtaining the hyperelastic properties of filled elastomers in finite strain applications.** Polymer testing, 41 (2015), pp. 44-54
[9] K. Venkatesh Raja, R. Malayalamurthi, **Assessment on assorted hyper-elastic material models applied for large deformation soft finger contact problems.** Int J Mech Mater Des 7, 299 (2011)
[10] A.F. Bower, **Applied Mechanics of Solids.** solidmechanics.org (2008)
[11] L.R.G. Treloar, 1948 Proc. Phys. Soc. **60** 135
[12] B. Kim, S.B. Lee, et al., **A comparison among neo-hookean model, mooney-rivlin model, and ogden model for chloroprene rubber.** Int. J. Precis. Eng. Manuf., **13** (5) (2012), pp. 759-764
[13] S.N.A.M. Noor, J. Mahmud, **Modelling and computation of silicone rubber deformation adapting neo-hookean constitutive equation.** Proceedings - 2015 5th International Conference on Communication Systems and Network Technologies, CSNT (2015), pp. 1323–1326
[14] E.M. Arruda, M.C. Boyce, A Three-Dimensional Constitutive Model for the Large Stretch Behavior of Rubber Elastic Materials. J. Mech. Phys. Solids **41** (1993) pp. 389-412
[15] M. Mansouri, H. Darijani, **Constitutive modeling of isotropic hyperelastic materials in an exponential framework using a self-contained approach.** Int. J. Solids Struct., 51 (25–26) (2014), pp. 4316-4326
[16] Q. Zhang, X. Li, Q. Yang, **Extracting the isotropic uniaxial stress-strain relationship of hyperelastic soft materials based on new nonlinear indentation strain and stress measure.** AIP Advances **8**, 115013 (2018)
[17] J. Bergstrom, **5 - Elasticity/Hyperelasticity.** Mechanics of Solid Polymers (2015), pp. 209-307
[18] M. Mooney, **A Theory of Large Elastic Deformation.** Journal of Applied Physics **11**, 582 (1940)

[19] R.W. Ogden, **Large deformation isotropic elasticity – on the correlation of theory and experiment for incompressible rubberlike solids.** Proc. R. Soc. Lond. A. **326**, (1984) pp. 565-584
[20] A. Das, V. Mathai, K. Breuer, **Nonlinear modeling and characterization of ultrasoft silicone elastomers.** Appl. Phys. Lett. **116**, 203702 (2020)
[21] **Hyperelastic behavior of rubberlike materials.** ABAQUS Analysis User's Manual, Dassault Systèmes (2007)